EUCLIPSE

EU Cloud Intercomparison, Process Study & Evaluation Project

Grant agreement no. 244067

Deliverable D3.7 Comparison of the hydrological and energy balance and the cloud amount as computed by ESMs.

Delivery date: 36 months

D3.7 "A comparison of the hydrological and energy balance and the cloud amount as computed by ESMs with field observations and satellite retrievals at selected locations – West Africa".

D. Bouniol – F. Guichard – O. Geoffroy – R. Roehrig
CNRM

As stressed by Roehrig et al. (2013, part of this delivrable), the regional response to global warming was uncertain in the models of the third phase of the Coupled Model Intercomparison Project (CMIP3 – Meehl et al. 2007) used for the Fourth Assessment Report (AR4) of the Intergovernmental Panel on Climate Change (IPCC), which even disagree on the sign of future rainfall anomalies over the Sahel (e.g., Biasutti and Giannini 2006; Lau et al. 2006). This disagreement remains even among models that reasonably simulate the twentieth-century West African climate (Cook and Vizy 2006). In fact, many of the previous generation climate models failed in capturing major features of the West African climatology and variability, and this casts serious doubt on the relevance of their climate projection in this region.
The purpose of the work undertaken in the framework of the EUCLIPSE project is to evaluate the ability of the current fifth phase of CMIP (CMIP5), a new ensemble of state-of-the-art climate models in simulating the present day climate over West Africa, focusing on the atmospheric energy and water cycle.

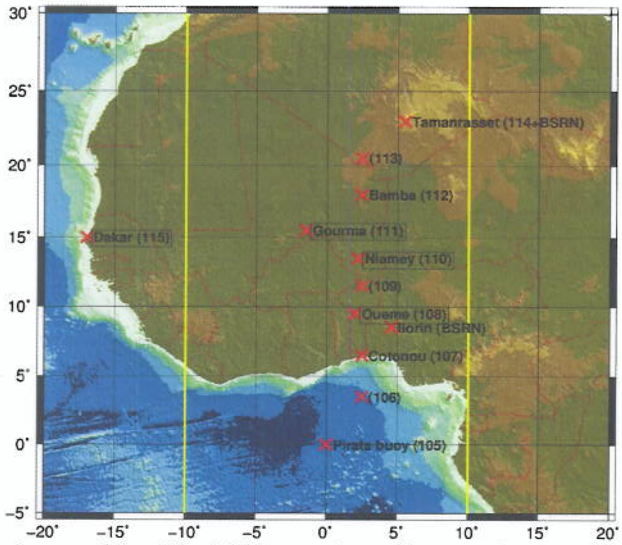

Figure 1 : *Geographical map of the West Africa region with superimposed the longitude limits of the meridian transect (vertical yellow lines) as well at the location of the cfSites (numbered according to the CFMIP convention).*

To do so, we take advantage of the data gathered together in the context of the AMMA program as well as recently launched satellite measurements. Complementary strategies are used for this evaluation, which articulate as follows :

- Taking into consideration major physical properties of the West African climate, in particular its strong zonal geometry, a regional evaluation of cloud and associated radiative properties may be performed as it appears meaningful. This analysis consists, following Hourdin et al. (2010), in zonally averaging between 10°E and 10°W (see figure 1, called in the following the meridional transect) either simulated fields or measurements, facilitating a quantitative comparison between them. Such a comparison also highlights potential meridional shifts in the large-scale structure of the West African Monsoon (for instance of the ITCZ and of the northern extend of the monsoon flow).
- As part of the Cloud Feedback Model Intercomparison Project (CFMIP) component of

CMIP5, 11 sites were defined along the meridional transect, and participating centers provided outputs at very high frequency (30 min) in order to better understand the climate model behaviors and their dependence on model formulation (Bony et al. 2011). The sites are numbered in Figure 1, and the ones for which a name is associated correspond to measurements sites of the AMMA program, note also the two BSRN sites. The high temporal resolution of the model outputs at these points allows to explore their variability at small temporal scales, and to assess their diurnal cycles.

Roehrig et al. (2013) enclosed several results regarding the evaluation of the ESM at the regional scale, which can be summarized as follow :

- the spread of the coupled-model projections in temperature and in precipitation in CMIP5 remains as large as in CMIP3;
- in SST-imposed mode (amip runs), almost all of the models capture the broad features of the West African monsoon, but with various degree of accuracy :
  - the averaged Sahel rainfall exhibits a large spread (+/- 50%);
  - the dispersion in surface air temperature is large over the Sahel and Sahara, and the simulation of the Saharan heat low and monsoon latitudinal position appear to be linked;
  - the meridional structure of the cloud cover, and its radiative impact, are tough challenges for CMIP5 models, leading to large biases in the surface energy balance, which are likely to feedback on the monsoon at larger scales;
  - the annual cycle exhibits a wide dispersion, pointing to the importance of physical processes in the seasonal dynamics of the West African climate;
  - the intermittence of precipitation over West Africa is large and only a few models reproduce it and more broadly the main features of intraseasonnal variability of convection there.

Bouniol et al. (2012) show that in addition to convective clouds, embedded in the ITCZ, this region is largely affected by other cloud types : low-level clouds, mid-level clouds and cirrus clouds underlying different genesis processes. All these clouds present a diurnal cycle that evolves throughout the monsoon season. Using radiative flux data from the Niamey site located in the Sahel, they also estimated with an empirical approach the cloud radiative effect at the surface for each individual cloud type. The largest reduction in incoming shortwave flux is found for the anvil category (between 200 and 300 W m^{-2}), low-level clouds and mid-level clouds both reduce the shortwave incoming flux by up to 150 W m^{-2}, and the impact of cirrus clouds may reach 50 W m^{-2}. In the longwave, the largest impact is found for mid-level and low-level clouds.
The fine-scale properties of clouds and associated precipitation have been evaluated in Roehrig et al. (2013). It appears that the wrong phasing of the diurnal cycle of precipitation still remains an issue, even though major improvements can be noticed in two models, and notably in the model of the IPSL (which is part of EUCLIPSE). However, most precipitation over the Sahel is provided by large mesoscale propagating systems, whose explicit representation in models is still lacking. Consistently with the diurnal cycle of precipitation, clouds associated with convection are shifted towards midday and display a too early minimum of the high-level cloud cover. However the results are contrasted among models, as models overestimating the frequency of rain occurrence are not necessarily those that overestimates the cloud frequency of occurrence at high levels, i.e. errors in the simulated cloud cover are not simply linked to biases in the representation of convective processes. The statistics of cloud fraction associated with the various cloud types are indeed very different from one model to another. Some models simulate only broken clouds for deep and mid-level clouds, whereas only high cloud fraction values are found in some others.
Geoffroy et al. (2013) refine, and extend to the top of the atmosphere the estimations of cloud radiative impacts presented in Bouniol et al. (2012). This study complements this previous work, in particular because it is based on a more physically-based approach of radiative processes, compared to the observationally-based empirical approach of Bouniol et al. (2012). Geoffroy et al. (2013) make use of the one-dimensional rapid radiative transfer model RRTM (Mlawer et al. 1997, Clough et al. 2005, Iacono et al. 2008), which is now used in several NWP and climate models. It

takes as inputs the measurements collected during the field experiment of the AMMA program; this includes atmospheric profiles of pressure, temperature and water vapour amount and surface radiative properties (albedo, emissivity), together with GERB radiation measurements at the top of the atmosphere. The strategy consists in using these data to simulate the clear-sky radiative fluxes with RRTM, and then to differentiate the computed fluxes with the measurements at the surface and at the top of the atmosphere. This yields an estimate of the cloud radiative effects. (Note that aerosol radiative effect are also taken into account in the clear sky calculation).

	Low-level clouds	Mid-level clouds	Cirrus	Anvil
Surface SW↓-SW↓cs	-40	-98	-31	-250
Surface LW↓-LW↓cs	7	12	2	15
TOA SW↑cs-SW↑	-37	-65	-19	-155
TOA LW↑cs-LW↑	9	32	31	74

Table 1 : *Estimation of the cloud radiative effect (CRE) in W m^{-2} at the top of the atmosphere (TOA, positive means less energy running away towards space) and at the surface (negative means the surface is loosing energy due to the presence of cloud) as a function of the cloud type in the shortwave and in the longwave domains. These estimations are for the Niamey site.*

It is notable that with this very distinct methodology, the values reported in Table 1 for the surface estimations are nevertheless in good agreement with Bouniol et al. (2012).

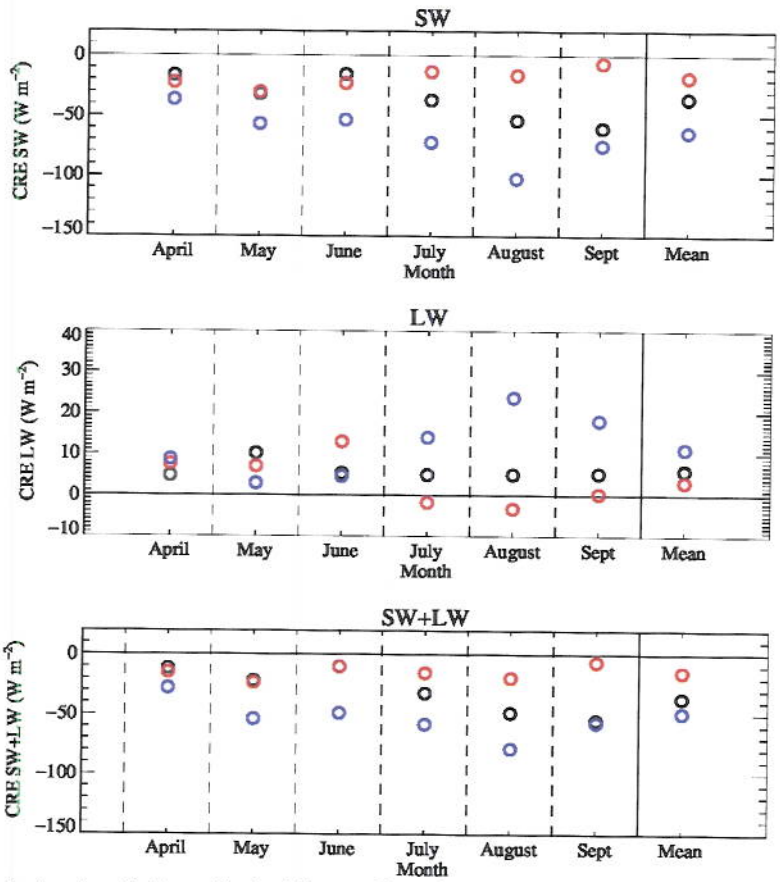

Figure 2 : *Seasonnal cloud radiative effect at the surface for the Gourma (red), Niamey (black) and Oueme (blue) sites in the shortwave (top), in the longwave (middle) and net (bottom).*

Geoffroy et al. (2013) made use of the measurements available at other sites along the transect and in particular the northern Sahelian Gourma and southern Soudanian Oueme sites (see Figure 1). In the shortwave domain, the cloud radiative effect is directly responding to the increase in cloud frequency of occurrence, as cloud occurrence is larger to the south of the studied region. The behavior in the longwave is more complex and probably involves an influence of changes in the clear sky properties within which clouds develop, the cloud radiative effect is also much weaker than in the shortwave. Given the accuracy of radiative flux measurements, it is not possible to elaborate too much on the smallest cloud radiative effect values, because they typically lie within the range of uncertainty of the measurements. During the wet period (july, august and september) the occurrence effect seems to dominate the contribution : the greenhouse effect is larger for the souther site (Ouémé). During the dry period (April to June), the effect is one order of magnitude smaller and the positive feedback appears stronger in the drier environment (Gourma or Niamey sites). This result point towards a peculiar behaviour of balance in the longwave domain between cloud occurring in more or less dry column.
Miller et al. (2012) computed the annual cloud radiative effect at the surface at the Niamey site and found larger order of magnitude for the cloud radiative effect. However their estimations arise from a very different methodology that may not well separate the cloud and aerosol radiative effect.

Finally the same separation by cloud types, as defined in Bouniol et al. (2012) has been applied in the models at the African sites. These results are illustrated in Figure 3 for the MPI-ESM-LR and HadGEM2-A models at the Niamey site.
The MPI-ESM-LR model presents a relatively correct order of magnitude of the cloud radiative effect at the surface except for the mid-level clouds whose radiative effect seems to be overestimated , presumably because of too reflective clouds. In contrast, the HadGEM2-A model, strongly underestimates the magnitude of the cloud radiative effect in the shortwave domain for all cloud types. This behaviour seems to results from its too thin clouds (i.e. low cloud fraction) and hence an overestimation of the incoming shortwave at the surface.

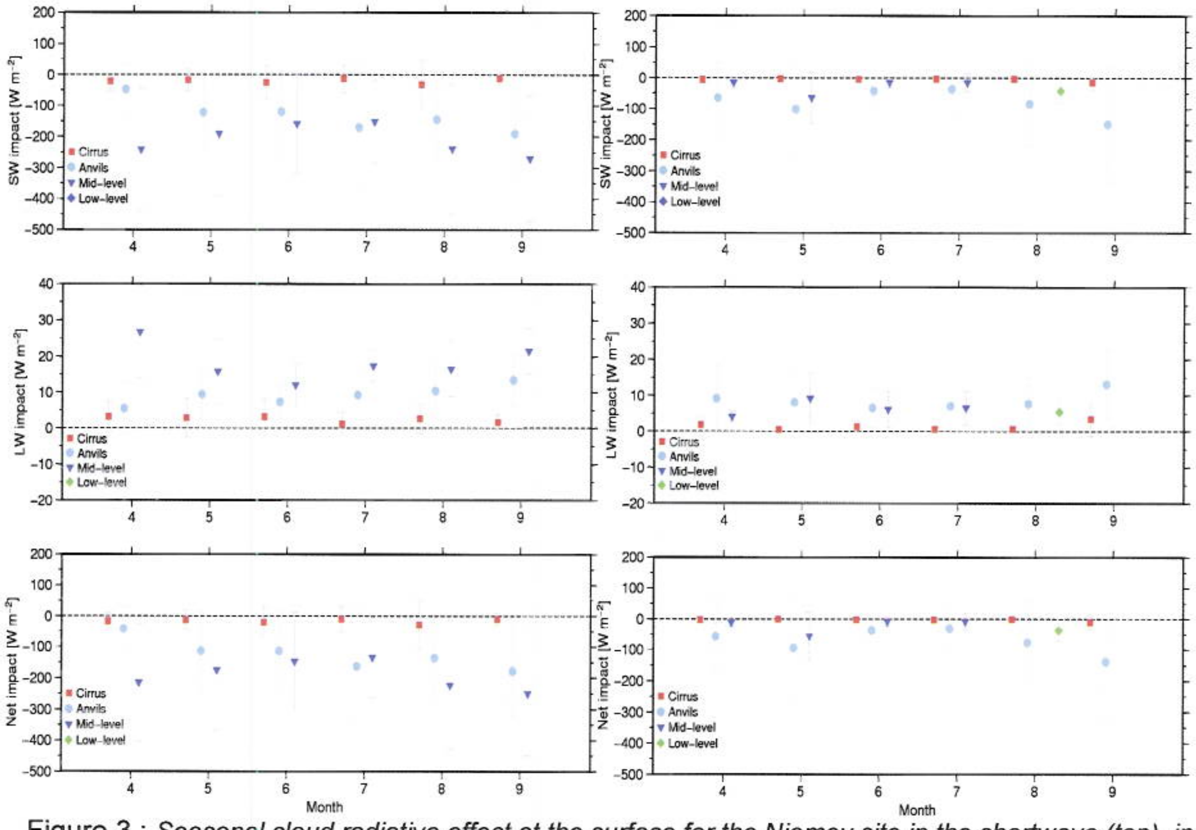

Figure 3 : *Seasonal cloud radiative effect at the surface for the Niamey site in the shortwave (top), in the longwave (middle) and net (bottom) for each cloud types in MPI-ESM-LR and HadGEM2-A2 models.*

As a summary, the work presented in this delivrable allowed to evaluate the behaviour of the ESM over a major continental region of the Tropics : i.e. West Africa. First, the transect strategy used to evaluate the model highlights meridional shifts of the synoptic patterns associated with the monsoon in some models. This knowledge and the configuration of the cfSites points (along a climatological transect) further allows to compare the high-frequency outputs of the model to surface based measurements in more climatological rather than strictly geographical corresponding locations. The collection of high-frequency outputs of the models appears as a powerful tool to understand the physical processes at play in cloud life cycles over this region. It also allows statistical and quantitative evaluations of key variables resulting from the parametrisations and that condition the magnitude of cloud feedbacks.
Beyond the results presented here, the components of the surface energy balance were found to widely vary among climate simulations (by several tens of W m^{-2} in monthly-mean values), and further work is ongoing to assess possible cloud radiative feedbacks on the surface energy balance, as the later is known to play a major role on the monsoonal circulations at larger scale. From this perspective, the COOKIE experiment appears well suited to advance on this issue.

References :

Biasutti, M., Giannini, A., 2006: Robust Sahel drying in response to late 20th century forcings. *Geophys. Res. Lett.*, **33**, L11706, doi:10.1029/2006GL026067.

Bony, S., Webb, M., Bretherton, C., Klein, S., Siebesma, P., Tselioudis, G., Zhang, M., 2011: CFMIP: towards a better evaluation and understanding of clouds and cloud feedbacks in CMIP5 models. *CLIVAR Exchanges No 56*, **16** (2), 20–24.

Bouniol, D., Couvreux, F. , Kamsu-Tamo, P.-H., Leplay, M., Guichard, F., Favot, F., O'Connor, E., 2012: Diurnal and seaonal cycles of cloud occurrences, types and radiative impact over West Africa. *J. Appl. Meteor. Climatol.*, **51**, 534–553, doi:10.1175/ 740 JAMC-D-11-051.1.

Clough, S. A., xShephard, M.W., Mlawer, E. J., Delamere, J. S., Iacono, M. J., Cady-Pereira, K., Boukabara, S., Brown, P. D., 2005: Atmospheric radiative transfer modeling: A summary of the AER codes. *J. Quant. Spectrosc. Radiat. Transfer*, **91**, 233–244.

Cook, K. H., Vizy, E.K., 2006: Coupled model simulations of the West African monsoon system: twentieth- and twenty-first-century simulations. *J. Climate*, **19**, 3681–3703.

Hourdin, F., et al., 2010: AMMA-Model Intercomparison Project. *Bull. Amer. Meteor. Soc.*, **91** (1), 95–104.

Geoffroy, O., Bouniol, D., Guichard, F., Favot, F., 2013 : Estimation of cloud radiative impacts over West Africa, seasonal and meridional patterns. In preparation, to be submitted to *J. Appl. Meteor. Climatol.*

Iacono, M. J., Delamere, J. S., Mlawer, E. J., Shepard, M. W., Clough, S. A., Collins, W. D., 2008: Radiative forcing by long-lived greenhouse gases: Calculations with the AER radiative transfer models. *J. Geophys. Res.*, **113**.D13103, doi:10.1029/2008JD009944.

Lau, K. M., Shen, S. S. P., Kim, K.-M., Wang, H., 2006: A multimodel study of the twentieth-century simulations of Sahel drought from the 1970s to 1990s. *J. Geophys. Res.*, **111**, D07111, doi:10.1029/2005JD006281.

Meehl, G. and Coauthors, 2007: Global Climate Projection. Climate Change 2007: The Physical Science Basis. Contribution of Working Group I to the Fourth Assessment Report of the Intergovernmental Panel on Climate Change, S. Solomon, D. Qin, M. Manning, Z. Chen, M. Marquis, K. B. Averyt, M. Tignor, and H. L. Miller, Eds., Cambridge University Press, Cambridge, United Kingdom and New York, NY, USA, 747–846.

Miller, M.A., Ghate, V.P., Zahn, R.K., 2012: The radiation budget of the West African Sahel and its controls: a perspective from observations and global climate models. *J. Climate.*, **25**, 5976-5996.

Mlawer, E.J., Taubman, S.J., Brown, P.D., Iacono, M.J., Clough, S.A., 1997: RRTM, a validated correlated-k model for the longwave. *J. Geophys. Res.*, **102**, 16,663-16,682.

Roehrig, R., Bouniol, D., Guichard, F., Hourdin, F., Regdelsperger, J.-L., 2013 : The present and future of the West African Monsoon : a process-oriented assessment of CMIP5 simulations along the AMMA transect. *J. Climate*, in press, March 2013.

The present and future of the West African monsoon: a process-oriented assessment of CMIP5 simulations along the AMMA transect.

Romain Roehrig * Dominique Bouniol, Francoise Guichard

CNRM-GAME, Toulouse, France

Frédéric Hourdin

LMD, IPSL, Paris, France

Jean-Luc Redelsperger

LPO, Brest, France

* *Corresponding author address:* Romain Roehrig, Météo-France, CNRM-GAME/GMGEC/EAC, 42 avenue G. Coriolis, 31057 Toulouse Cedex, France.

E-mail: romain.roehrig@meteo.fr

ABSTRACT

The present assessment of the West African monsoon in the models of the fifth phase of the Coupled Model Intercomparison Project (CMIP5) indicates little evolution since CMIP3 in terms of both biases in present-day climate and climate projections.

The outlook for precipitation in twenty-first-century coupled simulations exhibits opposite response between the westernmost and eastern Sahel. The spread in the trend amplitude remains however large in both regions. Besides, although all models predict a spring and summer warming of the Sahel, 10 to 50% larger than the global warming, their temperature response ranges from 0 to 7 K.

CMIP5 coupled models underestimate the monsoon decadal variability, but SST-imposed simulations succeed in capturing the recent partial recovery of monsoon rainfall. Coupled models still display major SST biases in the equatorial Atlantic, inducing a systematic southward shift of the monsoon. Because of these strong biases, the monsoon is further evaluated in SST-imposed simulations along the 10°W–10°E AMMA transect, across a range of timescales ranging from seasonal, intraseasonal and diurnal fluctuations.

The comprehensive set of observational data now available allows an in-depth evaluation of the monsoon across those scales, especially through the use of high-frequency outputs provided by some CMIP5 models at selected sites along the AMMA transect. Most models capture many features of the African monsoon with varying degrees of accuracy. In particular, the simulation of the top-of-atmosphere and surface energy balances, in relation with the cloud cover, and the intermittence and diurnal cycle of precipitation, demand further work to achieve a reasonable realism.

1. Introduction

During the second half of the twentieth century, Africa witnessed one of the largest interdecadal climate signal of the recent observational records. The severe drying of the Sahel, which culminated in the devastating drought of 1984, plagued the region from the 70's to the 80's (e.g., Nicholson 1980; Nicholson et al. 2000; Held et al. 2005). In the recent decade, the Sahel transitioned to a period with somewhat more abundant rainfall, suggesting a possible shift to a more favorable climate regime over the coming decades (Paeth and Hense 2004). However, at the same time, global mean temperature is increasing in response to increasing atmospheric greenhouse gases, so that predicting the evolution of Sahel rainfall from a range of a few decades to the end of the twenty-first century becomes urgently needed for developing adaptation strategies.

Such climate projections, as well as our physical understanding of the Sahel rainfall variability, mostly rely on general circulation models, characterized by a wide variety of complexity, from atmosphere-only models to the most recent Earth System Models (ESMs). The regional response to global warming was uncertain in the models of the third phase of the Coupled Model Intercomparison Project (CMIP3 – Meehl et al. 2007) used for the Fourth Assessment Report (AR4) of the Intergovernmental Panel on Climate Change (IPCC), which even disagree on the sign of future rainfall anomalies over the Sahel (e.g., Biasutti and Giannini 2006; Lau et al. 2006). This disagreement remains even among models that reasonably simulate the twentieth-century West African climate (Cook and Vizy 2006).

In fact, many of the previous generation climate models failed in capturing major features of the West African climatology and variability, damping our confidence in their climate projection. One of the reason is likely linked to the high spatial and temporal heterogeneities of the rainfall distribution across West Africa. In the Sahel, which lies at the northernmost extent of the West African monsoon (WAM), between 10°N and 20°N, precipitation is highly sensitive to the InterTropical Convergence Zone (ITCZ) latitudinal mean position during summer. There, rainfall is mainly supplied by mesoscale convective systems, often organized within synoptic disturbances such as African easterly waves (e.g., Kiladis et al. 2006).

Several studies emphasized the inability of current coupled or atmospheric models to correctly handle the main WAM characteristics. Cook and Vizy (2006) show that one third of CMIP3 models do not simulate a WAM system, i.e. they do not capture properly the summer northward migration of the ITCZ over the continent. Atmospheric regional and global models, forced by observed Sea Surface Temperatures (SSTs), analyzed within the framework of the AMMA-MIP[1], WAMME[2] and CORDEX[3]-Africa projects are generally more skillful, even though large biases in rainfall and the meridional circulation remain (Hourdin et al. 2010; Xue et al. 2010; Boone et al. 2010).

In the framework of the fifth phase of CMIP (CMIP5), a new ensemble of state-of-the-art climate models is now available (Taylor et al. 2012), and this raises several questions. Do they agree more on Sahel rainfall projections? Do they capture the partial rainfall recovery observed over the last decades? How well are they able to reproduce the main features of the WAM? In the following, the CMIP5 ensemble is used to address these questions, assess the results of the modeling community efforts and emphasize the challenges that remain for simulating the WAM. Our analysis indicates that over West Africa, CMIP5 models have not reached yet a degree of maturity which makes it possible to directly rely on them to anticipate climate changes and their impacts, especially with regards to rainfall.

The present study is also motivated by the recent progresses done in the observation and understanding of the WAM, thanks to the AMMA program (Redelsperger et al. 2006). The AMMA observational strategy (Lebel et al. 2010) documented a meridional transect extending from the Gulf of Guinea to the Sahara desert, along the Greenwich meridian. Three preexisting surface-observing super-sites along this transect were reinforced: the Upper Ouémé Valley, Niamey and Gourma AMMA-CATCH sites (e.g., Lebel et al. 2009). This

[1]The African Monsoon Multidisciplinary Analyses (AMMA) Model Intercomparison Project (Hourdin et al. 2010).

[2]West African Monsoon Modeling and Evaluation (Xue et al. 2010).

[3]the Coordinated Regional climate Downscaling Experiment (Jones et al. 2011; Nikulin et al. 2012)

transect was used within the AMMA-MIP framework to evaluate regional and global models (Hourdin et al. 2010).

As part of the Cloud Feedback Model Intercomparison Project (CFMIP) component of CMIP5, participating centers also provided output at very high frequency (30 min or model time step) on a series of 119 grid points around the world, in order to better understand the climate model behaviors and their dependence on model formulation (Bony et al. 2011). Among these sites, eleven were defined in coordination with the AMMA community along the AMMA transect, three of them corresponding to the super-sites mentioned above. In addition, the availability of new space borne measurements from active sensors as part of the A-train opens the path for the establishment of global climatologies of the three-dimensional distribution of clouds (e.g., Bouniol et al. 2012). The availability of these new datasets, new outputs at selected sites from CMIP5, as well as the better understanding of some key processes at work in the WAM system provides a unique opportunity to evaluate more in depth the WAM representation by climate models. In the present work, we seek to capitalize on this AMMA legacy, and to provide a process-oriented analysis of CMIP5 simulations.

The paper is organized as follows: section 2 describes the datasets used for the CMIP5 model evaluation. In section 3, the long-term variability of the WAM is assessed from CMIP3 to CMIP5 models. Section 4 evaluates the representation of the WAM mean state and seasonal evolution in both coupled and SST-forced simulations. Section 5 addresses a more physical evaluation of monsoon processes, with an emphasis on the intraseasonal and diurnal scales of the water cycle. Finally, conclusions are given in section 6.

2. Datasets

a. Climate models from CMIP3 and CMIP5

In the present work, we consider a wide range of output from climate models which participated to CMIP3 and CMIP5. Climate change scenarios of CMIP3 (SRES[4] A2) and of CMIP5 (RCP[5]4.5 and RCP8.5), in comparison with historical simulations (20C3M for CMIP3, Historical for CMIP5) are used to assess the West African monsoon response to an increase of the CO_2 atmospheric concentration. SST-imposed or AMIP[6]-type simulations are used to further analyze the representation of the WAM in the state-of-the-art models of the CMIP5 archive. Pre-industrial control runs (PiControl) with constant forcing are used for some CMIP5 models, to infer the decadal and interannual variability of Sahel precipitation.

A full description of the CMIP3 framework and a comprehensive assessment of the models can be found in Meehl et al. (2007). Integrations of 18 CMIP3 models are used here. They were made available to the community by the Program for Climate Model Diagnosis and Intercomparison (PCMDI) through their website (`www-pcmdi.llnl.gov/ipcc/model_documentation/ipcc_model_documentation.php`), where a detailed description of the models can be found.

The simulations performed as part of CMIP5 and used in the present study are listed in Table 1. They were made available on the Earth System Grid (ESG, `http://cmip-pcmdi.llnl.gov/cmip5/index.html`) data archive. The different types of integrations of the CMIP5 framework are described in Taylor et al. (2012). As we provide hereafter a more detailed evaluation of the CMIP5 AMIP simulations, Table 2 reports grid information of the atmospheric component of the models which provided this experiment.

[4]Special Report on Emissions Scenarios
[5]Representative Concentration Pathway
[6]Atmospheric Model Intercomparison Project

predicted by the ensemble mean over the Sahel west of 5°W whereas a wetting is predicted east of 5°W. The precipitation response remain qualitatively the same between CMIP3 and CMIP5, with a slight positive offset at the regional scale in the CMIP5 RCP8.5 scenario compared to CMIP3 SRES A2 scenario. Note that these two scenarios are distinct, so that the response amplitude in temperature and precipitation cannot be quantitatively compared. The inter-model standard deviation of the precipitation mean changes among the models is generally as large as the precipitation changes themselves.

The consensus on the westernmost Sahel ([15°W–5°W]) drying is relatively high, with about 80% of CMIP5 models agreeing on the sign of the change (Fig. 1.f). It was similar in the CMIP3 ensemble (Fig. 1.c). The drying remains moderate for most of the models, lower than 20% (Fig. 2.a). In contrast, the consensus on the wetting over the eastern West Sahel ([0°–10°E]) has been slightly reduced from CMIP3 to CMIP5 (Figs. 1.c, 1.e and 2.b), while it has clearly increased over the central/eastern Sahel ([10°E–35°E]), with now more than 75% of the CMIP5 models agreeing on the positive sign of precipitation changes (Figs. 1.c, 1.e and 2.c). The apparent low sign agreement in the transition region between the westernmost Sahel and the eastern West Sahel is likely related to the weak projected precipitation changes there. Note that the choice of the three averaging domains (Fig. 2) was conveyed by the sign agreement of the precipitation changes (Fig. 1) and some previous works that defined homogeneous regions over the Sahel at interannual to multidecadal timescales (e.g., Ward 1998; Lebel and Ali 2009). For some models, it might not be the most appropriate, in particular for those that do not capture the right position of the summer ITCZ (see section 4). A more detailed analysis of the projections is required but remains out of the scope of the present study.

East of 0°E, the CMIP5 ensemble mean precipitation response is partly dominated by about 4-5 models that simulates a strong increase of precipitation, greater than 60%. Those models also predict a relatively weak warming over the Sahel, and even some cooling for one of them over the eastern Sahel. In the RCP8.5 scenario, their JAS values of (ΔT_{2m},

$\Delta Pr/Pr$) over the central/eastern Sahel are (2.9 K, 62%) for MIROC5, (0.2 K, 86%) for BNU-ESM, (0.2 K, 103%) for FGOALS-g2, (-1.0 K, 103%) for MIROC-ESM and (2.7 K, 109%) for MIROC-ESM-CHEM, while the values of all other models range in (4.5±1.5 K, 0±30%). Most projections thus indicate moderate changes in the pessimistic scenario, to be compared with the 40% decrease observed between the 50-60's and 70-80's, and the +20% rainfall recovery in recent years over parts of the Sahel (Lebel and Ali 2009).

The temperature and precipitation changes are likely related. Reinforced rainfall should moderate the temperature increase in summer, through an increase of surface latent heat flux. Figures 2.e and f are consistent with this interpretation. In the dry March-April-May season, the Sahel warming reflects mostly an amplification of the global warming response by 30 ±20%. In contrast, the projected summer Sahelian warming displays much more spread than the global warming, emphasizing a coupling with the rainfall response. Three models, which predict a significant increase of Sahel rainfall, also predict a much weaker JAS warming than the global value.

b. Decadal and interannual rainfall variability over the Sahel

The Sahelian rainfall exhibits a large variability at decadal and interannual timescales. In order to address these scales, the time series of the Sahel precipitation P was decomposed into a decadal component $\overline{P}^9$ and an interannual fluctuation δP, such as $P = \overline{P}^9 + \delta P$. $\overline{P}^9$ is defined as the 9-year running mean of the raw series. Fig. 3.a illustrates the observed raw and filtered time series of precipitation averaged over [10°N–18°N, 0°–10°E], for both the CRU and CMAP datasets (see Table 3). The Sahelian drought is clearly identified after 1973, with a partial recovery in the recent years. Although this recovery is not homogeneous over the entire Sahelian belt, Lebel and Ali (2009) show a clear signal over this central Sahel domain.

The skill of CMIP5 models to reproduce this recent recovery is addressed in AMIP simulations through the computation of precipitation mean difference between the periods

2000-2008 (wetter) and 1979–1987 (drier – Fig. 3.b, dots). The relative change between these two periods ranges between 10% in the CRU dataset and 24% in the CMAP dataset. Despite a large dispersion, one half of the models capture the tendency to rainfall recovery. Five have a tendency close to zero and three even simulate a significant negative tendency. This might be partly due to internal variability as illustrated with the five members of the IPSL-CM5A-LR AMIP ensemble (Fig. 3.b), which predicts a recovery, ranging from +6% to +21%.

The reasonable skill of the AMIP simulations is probably related to the monsoon response to the change of SSTs, consistently with the success of several atmospheric models to reproduce the main outlines of the twentieth century Sahel rainfall (e.g., Tippett and Giannini 2006; Hoerling et al. 2006).

The standard deviation of $\overline{P}^9$ in the PiControl and Historical experiments can be used to assess the skill of coupled atmosphere-ocean models to reproduce the observed decadal variability (Fig. 3.b). In CRU observations, the standard deviation over the twentieth century reaches almost 10%. Most models underestimate this amplitude, often by a factor of two, in both types of experiments, with the notable exceptions of IPSL-CM5B-LR, which significantly overestimates the amplitude of the decadal variability, and of BCC-CSM1.1, which has an amplitude slightly higher than the observed one. It is also remarkable that the amplitude of decadal variability is highly consistent for each model across the two experiments, suggesting that decadal fluctuations in Historical runs are not forced by greenhouse gases, aerosols or land-use (for models including land-use changes).

Interannual variability of CMIP5 models is investigated based on the standard deviation of the interannual fluctuations δP (Fig. 3.c). The observed value of 12% is consistent in CMAP and CRU observations. In the Historical and PiControl simulations, all models lie between 8% and 17%, except ACCESS1.3 (22%), BCC-CSM1.1 (30%), CMCC-CM (22%), FGOALS-s2 (22%), IPSL-CM5B-LR (38%), and MRI-CGCM3 (20%) which overestimate interannual variability. The large amplitude of decadal variability in BCC-CSM1.1 and

IPSL-CM5B-LR may be a consequence of this excessive year-to-year variability.

4. The representation of the West African monsoon mean state from CMIP3 to CMIP5

Most of the following analysis is based on the 10°W–10°E AMMA transect, promoted by the AMMA observing strategy (Lebel et al. 2010) and the AMMA-MIP framework (Hourdin et al. 2010). Due to the little zonal variations in surface field meridional structure between 10°W and 10°E, this transect approach is well suited to analyze the WAM climatological structure. As a consequence, the term "Sahel" will be used hereafter in a *limited meaning* for the 10°–18°N, 10°W–10°E region. As shown above, such a framework is not as appropriate to study the WAM interannual-to-long-term variability.

a. Precipitation bias in historical simulations and its relationship with surface air temperature

The sensitivity of the Sahelian rainfall to SSTs has important consequences on the skill of climate models to simulate properly the present-day mean state of the monsoon system. All coupled models suffer from significant and robust SST biases with respect to their AMIP version (Fig. 4). Most of them systematically display strong warm biases (of several K) over upwelling regions, on the eastern side of tropical oceanic basins, especially in the south Atlantic. The only exception is CSIRO-Mk3.6.0, which has a global cold bias over the ocean.

The CMIP5 ensemble mean warm bias (CMIP5–ENSEMBLE in Fig. 4) peaks at more than +3 K in the equatorial eastern Atlantic, contrasting with a cold bias of about -1 K in the North Atlantic. This systematic bias structure is remarkably similar to the CMIP3 ensemble mean (CMIP3–ENSEMBLE in Fig. 4).

This warm bias in the equatorial Atlantic has been shown to be partly responsible for the systematic southward shift of the ITCZ in coupled models (Richter and Xie 2008). It is associated with a strong reinforcement of rainfall over the Guinean coast and often a reduction over the Sahel, as illustrated in Fig. 4. Consistently, CSIRO-Mk3.6.0 shows an opposite signal, with slightly less rainfall over the Guinean coast.

The latitudinal position of the ITCZ over West Africa is, to some extent, related to the intensity of the north-south temperature gradient, which is partly driven by the SSTs in the equatorial Atlantic (Fig. 5). The correlation coefficient reaches 0.4 in Historical CMIP5 simulations. AMIP simulations exhibit a similar relationship, with a smaller spread in the ITCZ position. The temperature over the Sahara is thus expected to play an important role too in the summer monsoon position. It will be further evaluated in section 4.b.2.

To summarize, both CMIP3 and CMIP5 coupled models exhibit large biases in the mean position of the west African monsoon, which is likely associated with the warm SST bias in the equatorial Atlantic. This first-order, robust and quasi-systematic bias prevents any further insight into the representation of key features and processes of the monsoon in coupled simulations. Therefore, we now focus on AMIP simulations, which display a weaker dispersion in the ITCZ summer position over West Africa (Fig. 5).

b. The WAM mean state in AMIP simulations

1) Precipitation

Figure 6 shows JAS precipitation averaged from 1979 to 2008 between 10°W and 10°E for each model and observational dataset introduced in section 2. Even though the GPCP and TRMM datasets do not cover the same period, they provide similar results along this transect, the sensitivity to the exact chosen period being much smaller than the typical model biases (not shown). Following the previous section and Fig. 5, models have been separated into two subsets according to their mean temperature over the Sahara: the warm (Fig. 6.a) and the cold (Fig. 6.b) models. Overall, models capture the large-scale precipitation maximum over the continent near 10-11°N. About one third of the models (BCC-CSM1.1, FGOALS-s2, GISS-E2-R, HadGEM2-A, INM-CM4, the three IPSL-CM5 models and MRI-CGCM3) locate their ITCZ a bit too much to the south, near 7-8°N. In contrast, only a few models reproduce the maximum amount of precipitation along the transect (8 mm day^{-1}). Five models overestimate this maximum by 1.5 to 4 mm day^{-1} (CSIRO-Mk3.6.0, GFDL-HIRAM-C180, GFDL-HIRAM-C360, IPSL-CM5A-MR and MIROC5). Seven models underestimate it by 1 to 5 mm day^{-1}. Thus, only half of CMIP5 models are in qualitative agreement with observations. About one half of the models underestimate the rainfall over the Sahel, i.e. north of 12°N, and most of these "too dry" models are also among the colder ones.

The high-resolution runs of GFDL-HIRAM (see Table 2) capture the monsoon latitudinal structure, but exhibit similar skills to other models in reproducing the amplitude of precipitation. Besides, little sensitivity to the passage from a 0.5° (GFDL-HIRAM-C180) to a 0.25° (GFDL-HIRAM-C360) resolution is noticed. Enhanced vertical resolution from MPI-ESM-LR (47) to MPI-ESM-MR (95) results in a very similar ITCZ. In contrast, the modification of the physical packages from IPSL-CM5A-LR to IPSL-CM5B-LR indicates a clear dependence on the formulation of the model physics, especially north of 10°N, where rainfall is decreased by almost a factor of two in IPSL-CM5B-LR.

2) Temperature at 2 m and the Saharan Heat Low

The spread described in the previous section can be partly related to the meridional large-scale temperature gradient (section 4.a, Fig. 5). In AMIP simulations, this gradient is driven at first order by the temperature in the Saharan heat low region, which is a key feature of the west African monsoon at the seasonal (Lavaysse et al. 2009) and intraseasonal (Chauvin et al. 2010) timescales. During the summer, a heat low establishes a low pressure system over the Sahara desert, and acts to reinforce the moist monsoon flow over the Sahel. The Saharan heat low is also key in the maintenance of the African easterly jet in the mid troposphere (Thorncroft and Blackburn 1999). The associated temperature gradient is a source of baroclinic energy for African easterly waves, which affects rainfall at various timescales (e.g. Fink and Reiner 2003; Kiladis et al. 2006; Thorncroft and Rowell 1998). In particular, Ruti and Dell'Aquila (2010) showed that models characterized by a weak meridional temperature gradient are unable to feed these synoptic disturbances. A strong gradient is however not a necessary condition for arising waves.

Over the Sahara, the near-surface temperature in CMIP5 models exhibit a large spread, which reaches almost 7 K near 25°N (Fig. 7). This spread starts to develop in the southern Sahel, around 10°N, and extends up to the northern coast of Africa at 35°N. Unfortunately the dispersion is as large as in observational datasets and reanalyses. This reflects the sparse coverage of in-situ observations over the Sahara, and precludes detailed model evaluation there. The surface energy budget over the Sahara discussed at the end of this section provides further insight into the origin of this spread within the CMIP5 ensemble. Up to 15°N, observations and reanalyses are in better agreement and the spread among models is weaker, although about one third of CMIP5 models are still too cold by 2-3 K (BNU-ESM, CCSM4, CESM1(CAM5), CNRM-CM5, EC-EARTH, GFDL-HIRAM-C180 and -C360, MRI-AGCM3.2S, NorESM1-M), and one too warm by 2-3 K (MRI-CGCM3).

3) Clouds and their radiative effect

Bouniol et al. (2012) analyzed the cloud cover mean properties over the Sahel with the AMF data of Niamey. They identified four cloud categories: cloud associated with convective systems, and low-, mid- and high-level clouds, in agreement with Slingo (1980). Using CloudSat and CALIPSO, they also documented their seasonal cycle at the regional scale over West Africa, characterized by: a northward migration of deep convective clouds associated with the ITCZ, low-level shallow clouds over the Sahel in summer and the ubiquitous presence of mid-level and cirrus clouds. In addition, a 2-km-deep layer of stratocumulus is observed over the Gulf of Guinea. Figure 8 (first panel) presents the JAS climatological latitude/altitude cross-section of the mean cloud fraction, built from five years of CloudSat-CALIPSO data. Note that the precipitating water phase was discarded in the observations.

All the models capture to some extent the observed cloud structure (Fig. 8). The maximum in cloud fraction related to the deep convective systems is collocated with the mean ITCZ position (Fig. 6), although some models do not reproduce the observed vertical extent of cloud fraction. Most models include in their cloud fraction only non-precipitating condensed water, whereas in the observational dataset, the computed cloud fraction also accounts for precipitating particles, especially above the freezing level. Even dense aggregates found in convective anvils need about 50 minutes to fall down from the 8-km altitude to the freezing level at a 1 m s^{-1} fall speed (Bouniol et al. 2010). The apparent underestimation of cloud fraction in the mid-troposphere, in ACCESS1.3 or IPSL-CM5A-LR, may thus partly originate from the lack of consideration given to precipitating ice as making part of the cloud (Waliser et al. 2011).

The high amount of mid-level clouds between 15°N and 30°N is a specificity of the region. However, none of the models manage to reproduce the observed amount, even if some of them (CanAM4, IPSL-CM5B-LR, MIROC5) partly capture their occurrence. The stratocumulus over the Gulf of Guinea are also challenging most of the models. They are often not deep enough when they occur, and CNRM-CM5 and CanAM4 completely miss this cloud type.

The proper representation of these different cloud types is important for the regional energy budget and associated cloud feedbacks. Figure 9 shows the cloud radiative effect (CRE) at the top of the atmosphere. The longwave CRE is strongly shaped by the convective cloud cover amount and vertical structure, and the latitudinal shift of its maximum is clearly explained by the spread of the ITCZ JAS location (Fig. 6).

The shortwave CRE displays two minima associated with the stratocumulus clouds over the ocean and the ITCZ over the continent. The CRE spread across the simulations is larger in the shortwave than in the longwave. Most models overestimate this shortwave CRE over the ocean, except CNRM-CM5 due to a lack of stratocumulus clouds there (Fig. 8). Further north, within the ITCZ, the two IPSL models and HadGEM2-A underestimate the CRE, and IPSL-CM5A-LR shows little response to the cloud cover increase with latitude.

Even though shortwave and longwave CRE partly compensate each other, they have a distinct latitudinal structure. The longwave CRE maximum is shifted 5°-northward compared to the shortwave CRE minimum. As a result, the observed net CRE is negative south of the ITCZ, where the shortwave component is dominant, and turns to slightly positive values north of the ITCZ, where the longwave component dominates. Over most of the Sahel and Sahara, mid-level and convective clouds have a positive net CRE. Thus the CRE provides locally more favorable conditions for the development of convection in the Sahel than further south during the monsoon (Chou and Neelin 2003). Only one half of the models capture the Sahelian band of positive net CRE, but no model reproduces accurately its meridional structure, with the right balance between the shortwave and longwave components. North of the ITCZ, the CRE is generally too small, and to the south the spread is very large.

4) Incoming radiation at the surface

Incoming radiative fluxes at the surface are important components of the surface energy budget, with the advantage that they can be reasonably evaluated with a joint utilization of in-situ AMMA measurements and satellite products. Their understanding is complex as they undergo the influence of the whole troposphere thermodynamical state, the vertical distribution of cloud properties, and the aerosol loading. During the monsoon season, the latter is expected to impact less the ITCZ region as aerosols are scavenged by precipitation. However they strongly affect the Sahara region (Knippertz and Todd 2012).

At the surface, the JAS shortwave incoming flux meridional gradient is large, reaching more than 100 W m^{-2} from the Guinean coast to the Sahara (Fig. 10), and involving a strong CRE. These variations are not accurately simulated, with JAS-mean departures from observations larger than several tens of W m^{-2}. Over the Guinea coast, more than one half of models underestimate the incoming surface shortwave flux in response to a too thin and reflective cloud layer. Within the ITCZ, the IPSL models and HadGEM2-A strongly overestimate this radiative flux. As it will be shown in section 5.b.2, these two models display a reasonable cloud frequency of occurrence, but they both systematically underestimate the cloud fraction (Fig. 18) . Over the Sahara, most of the models overestimates the incoming surface shortwave flux, in particular the colder ones (Fig. 10.b). Figure 8 pointed there a clear deficit of mid-level cloudiness, which has a strong impact in the shortwave (Bouniol et al. 2012). The representation of aerosols may also explain a large part of the spread.

Meridional fluctuations of the longwave incoming radiation at the surface are weaker. It increases from the more humid and cloudier Gulf of Guinea to the drier Sahara at 20°N by 10-20 W m^{-2}. Note however that the atmosphere warms and loads with aerosols along this direction. Several models simulate this weak gradient, with departures less than 20 W m^{-2}. Further north, biases in the longwave incoming surface radiation increase significantly and reach the same order of magnitude as in the shortwave, especially in the colder models (Fig. 10.d). The lack of mid-level clouds may partly explain the underestimation. Further investigations are needed to better understand the origin of the spread.

Over this dry region, feedbacks with surface air temperature is investigated in models in Fig. 11. Opposite behaviors are noted with increase (decrease) in the temperature as the longwave (shortwave) increases with a higher correlation in the longwave domain. Figure 11.c shows that the higher the incoming shortwave, the lower the incoming longwave. Since most models simulate a cloud free troposphere in a relative dry environment, this suggests important roles of the surface albedo and of the aerosol loading (Kothe and Ahrens 2010) in the spread over the Sahara. Radiative transfer calculations would help in better identifying the sources of discrepancies between models over the region.

c. *The seasonal cycle of the WAM*

At the seasonal timescale, the West African monsoon is characterized by a northward migration of the ITCZ with an abrupt climatological shift in early summer (Sultan and Janicot

2000, 2003), culminating in August, and by a smoother southward withdrawal of the rainfall band in September and October. The monsoon onset time is consistent in the two observational datasets (Fig. 12.a and b). It is well marked by a transition between a maximum of precipitation along the Guinean coast in May-June and a second one centered near 12°N in August. In-between, a minimum of rainfall occurs over the whole region as the ITCZ moves northward. Presumably because the monsoon is primarily forced by the annual excursion of the sun, most of models capture the ITCZ summer migration, however with varying degrees of accuracy. Four models do not reproduce the spring precipitation maximum near the Guinea coast (FGOALS-g2, INM-CM4, IPSL-CM5A-LR and -MR), while six overestimate it (CNRM-CM5, CSIRO-Mk3.6.0, GFDL-HIRAM-C180 and C360, MPI-ESM-LR and MR). The monsoon is almost inexistent in BCC-CSM1.1, very weak in FGOALS-s2 and rather weak in HadGEM2-A, IPSL-CM5B-LR, MPI-ESM-LR and MR and MRI-CGCM3, consistently with Fig. 6. When simulated, the onset occurs at approximately the correct time of the year, as in CNRM-CM5, CSIRO-Mk3.6.0, the two versions of GFDL-HIRAM, the two versions of MPI-ESM, and NorESM1-M. For three models (CNRM-CM5, CSIRO-Mk3.6.0 and FGOALS-g2), the 1-mm isoyet reaches latitudes above 20°N, which is observed neither in TRMM nor in GPCP. On the opposite, four models simulate rain over the Gulf of Guinea south of 0°N during the summer (INM-CM4, IPSLCM5A-LR, IPSL-CM5A-MR and IPSL-CM5B-LR).

The annual cycle of temperature over West Africa is also characterized by a northward migration of the temperature maximum during spring and summer and a southward retreat at the end of August (Ramel et al. 2006). Two annual maxima can be identified (Fig. 13.a). The first one occurs over the Sahel during May-June, prior to the monsoon rainfall onset, when the soil is still very dry, and typically at the time of the establishment of a humid low-level monsoon flow in the Sahel (Slingo et al. 2009; Guichard et al. 2009). Then, the summer rainfall over the Sahel leads to enhanced surface evapotranspiration (Timouk et al. 2009) and to an overall cooling at the surface. The second maximum occur over the Sahara, near 27-28°N at the end of July, one month after the insolation maximum.

The annual cycle depicted by the CRU, ERA-Interim and MERRA (not shown) datasets is very consistent. It is noticeable that the NCEP-CFSR reanalysis is generally colder by 2 K over the Sahel (not shown). This perhaps surprising result is nevertheless fully consistent with recent comparisons performed over land (Wang et al. 2011; Bao and Zhang 2012).

Very large spread is found among AMIP simulations all year long. They are particularly pronounced outside of the monsoon summer season. Although most of the models simulate the northward displacement of maximum temperature from winter to summer, the spread over the Sahel reaches up to 6 K in winter and none of them captures the spring maximum over the Sahel, except to some extent BNU-ESM and HadGEM2-A. In half of the models, the amplitude of the temperature annual cycle is lower than in CRU. Some models such as BCC-CSM1.1, HadGEM2-A, INM-CM4, IPSL-CM5 models, MRI-CGCM3 do not form a strong heat low over the Sahara, which is consistent with an ITCZ that fails in migrating northward during the summer (Fig. 12).

5. Towards a physical evaluation of the WAM in AMIP simulations

The previous section addressed basic large-scale features of the west African monsoon. Higher-frequency fluctuations and finer-scale processes are now evaluated. These scales are indeed crucial to improve food management and disaster mitigation in the region (e.g., Sultan et al. 2005), and their evolution in the climate change perspective is key for adaptation policies. Their representation by state-of-the-art climate models is a major target if they are to be trustworthy for simulating either present-day climate or the impact of global warming over West Africa.

a. Intraseasonal variability of precipitation

Rainfall over West Africa is highly intermittent in space and time. The rainy season is punctuated by dry and wet periods occurring at various intraseasonal timescales (Janicot et al. 2011). Three preferred timescales have been highlighted: around 40 days, probably involving the Madden-Julian Oscillation (Mathews 2004, Janicot et al. 2009), approximately 15 days with two main regional modes (Mounier and Janicot 2004; Mounier et al. 2008; Janicot et al. 2010; Roehrig et al. 2011), and in the 3-10-day range with the well-known African Easterly Waves (AEWs – e.g., Kiladis et al. 2006). In the present study, we do not address specifically each of these intraseasonal scales. In contrast, we give a brief overview of the main properties of convection at intraseasonal timescales, which, from this perspective, makes West Africa a unique place in the world.

Figure 14 indicates the variance of OLR filtered in the 1-90-day range. OLR is preferred to precipitation here because precipitation variance is closely related to its mean value, so that differences in precipitation variance in models are mainly attributed to bias in precipitation mean state. A zonally-elongated maximum of OLR variance (> 1000 W^2 m^{-4}) is observed over the Sahel, along the northern side of the ITCZ. When reaching the Atlantic ocean, the band moves southward, up to 10°N. Intraseasonal variance is slightly weaker (900 W^2 m^{-4}) over the eastern Sahel and Central Africa. Very few models capture the observed structure and amplitude over the Sahel. GFDL-HIRAM-C180 and C360, MRI-CGCM3 and NorESM1-M overestimate the amount of intraseasonal variability, with a maximum rather collocated within the ITCZ. The southward slope in the east-west direction is generally reproduced. However, about one half of CMIP5 models underestimate the intraseasonal variability of deep convection. Some of them have a variance reaching one third of that observed, when averaged over the domain [5N-20,10W-10E] (Fig. 15.a). These results are very similar to those obtained with the CMIP3 models (Roehrig 2010).

The observed distribution of the OLR intraseasonal variance is captured by none of the models (Fig. 15.b). The 10-90-day scale (black bars) explains 20% of the intraseasonal variability in only four models (GFDL-HIRAM-C180 and C360, FGOALS-g2 and MIROC5), while it is overestimated by more than 10% in the others. Overall, models with underestimation of OLR intraseasonal variance put too much weight in long timescales. The 3-10-day synoptic timescale (white bars) corresponds to about 50% of the observed intraseasonal variance. All models reproduce this amount at an accuracy of ±10%, indicating that they are likely able to simulate AEW-like variability (Ruti and Dell'Aquila 2010). However, even though convection can be organized at the synoptic or intraseasonal scales, most of summer rainfall over West Africa is provided by a very few heavily-precipitating mesoscale convective systems (Mathon et al. 2002). As a consequence, precipitation is highly intermittent from day to day and has very little persistence over the Sahel. Consistently with the fact that models have difficulties to represent such convective systems (see also section 5.b.1), none of them capture the very high-frequency (1–3 days, grey bars) proportion of almost 30%. Even the high-resolutions GFDL-HIRAM-C180 and C360 runs reach only 20% in this band.

This notion of persistence can be quantitatively characterized by the autocorrelation function of precipitation. Using it, Lin et al. (2006) showed that the Madden-Julian Oscillation variance in most of CMIP3 models comes from an overreddened spectrum, associated with too strong persistence of equatorial precipitation. In that regard, rainfall over Africa has relatively unique properties. There, precipitation at the 2.5°x2.5° grid-point scale is very similar to a white noise, with a 1-day lag autocorrelation even slightly negative in some places (Fig. 16.a). There is no persistence at all at the local scale. No region around the world behaves similarly, either in boreal summer (Fig. 16.a) or in boreal winter (Fig. 16.b), except to some extent the northern part of South America. Fig. 16.c confirms that such a property of the west African monsoon remains a challenge for most of state-of-the-art models. GFDL-HIRAM-C360 reaches the closest value to zero (0.06), and is closely followed by GFDL-HIRAM-C180 (0.09), FGOALS-g2 (0.09) and MIROC5 (0.12).

The relative success of the GFDL-HIRAM models might be partly attributed to their high spatial resolution. The correct behavior of MIROC5 is possibly related to the effort undertaken to make the convective scheme more sensitive to dry air in the free troposphere (Chikira and Sugiyama 2010), and which eliminates the artificial triggering function[7] for deep convection used in the previous version (CMIP3) of the MIROC model and based on the work of Emori et al. (2001). In CMIP3, miroc3.2(medres) and miroc3.2(hires) had a similar behavior to MIROC5 with regards to this diagnostic (Roehrig 2010). The CMIP3 MRI model (mri_cgcm2.3.2a) which was sharing the same convective parameterization (Pan and Randall 1998), except for this artificial triggering, produced too much persistence of precipitation over West Africa.

b. The diurnal cycle at selected AMMA sites

The CMIP5 archive contains for a few AMIP simulations a large set of diagnostics at high-temporal frequency, for ten grid-points along the west African transect. These high-frequency output allow to evaluate fine-scale processes.

1) PRECIPITATION

Rain over West Africa is mainly of convective origin (Mathon et al. 2002). Convective system properties (size, lifecycle, organization) strongly depend on latitude leading to different characteristics of the diurnal cycle of precipitation. Figure 17 illustrates such differences between two sites distant from less than 500 km in the North-South direction: the Ouémé site (9.5°N), just along the southern fringe of the ITCZ, and the Niamey site (13.5°N). The southernmost site presents a bimodal diurnal cycle with a first peak around 1800 UTC and a smaller one between 0300 and 0600 UTC. Further north, only the morning peak remains. Over Niamey, about 80% of the annual rainfall is produced by westward propagating systems (Dhonneur 1981), initiated in the afternoon over the elevated terrain of northeastern Niger

[7] The triggering of deep convection occurred only when the relative humidity averaged over the vertical went over a given threshold (~80%)

located several hundreds of kilometers eastwards and reaching the Niamey region in the early morning (Rickenbach et al. 2009). South of the ITCZ, the contribution of propagating systems decreases to 50% (Fink et al. 2002; Depraetere et al. 2009), and a more common late afternoon peak arises. This bimodal structure observed here is consistent with the secondary nighttime peak emerging from global datasets (Yang et al. 2008).

To our knowledge, no model explicitly includes a proper representation of propagating mesoscale convective systems such as squall lines, so that they are not expected to capture the diurnal cycle of precipitation over Niamey. Indeed, Figure 17 illustrates that the precipitation distribution of the models is qualitatively very similar between the two sites. The variations between the two sites are related to a more seldom occurrence of rain events at higher latitudes. This accounts for the differences in the distribution of the two IPSL models. As a consequence, the use of the Ouémé site as a reference appears more suitable for evaluating the diurnal cycle of rainfall over West Africa (Fig. 17), at least until models can properly represent propagating convective systems.

Consistently with previous studies (Betts and Jakob 2002; Guichard et al. 2004), the distribution of precipitation in CMIP5 models peaks in afternoon. A first group of models (CanAM4, CNRM-CM5, IPSL-CM5A-LR, HadGEM2-A and MPI-ESM-LR) display a too early peak of precipitation, between 1200 and 1500 UTC, roughly in phase with insolation. More recently, Nikulin et al. (2012) showed that the same issue affects regional climate models of the CORDEX-Africa experiments, despite their finer resolution (around 50 km). This incorrect timing of rainfall impacts on the surface water and energy budgets in various ways (Del Genio 2011).

In the two remaining models (IPSL-CM5B-LR and MRI-CGCM3), the precipitation maximum occurs later, between 1500 and 1800 UTC, more in phase with observations. The difference between IPSL-CM5A-LR and IPSL-CM5B-LR in particular attests of recent progress on this long-standing issue. Rio et al. (2012) and Sane et al. (2012) discussed this improved behavior of IPSL-CM5B-LR, which they attributed to a more realistic description of thermal plumes in the boundary layer (Rio and Hourdin 2008), the introduction of a parameterization of convective cold pools (Grandpeix and Lafore 2010) and an improved closure and triggering for convection (Rio et al. 2012).

There is also a large spread in the amplitude and intensity of this afternoon maximum, hence affecting the distribution of rain intensity (Fig. 17). Most models present a maximum frequency of occurrence for an intensity near 1 mm h^{-1}, reaching even larger values in MPI-ESM-LR. In the remaining part of the diurnal cycle, rain intensity decreases by one to two orders of magnitude in IPSL-CM5A-LR, IPSL-CM5B-LR, HadGEM2-A or MPI-ESM-LR, and by less than one in CanAM4, CNRM-CM5 or MRI-CGCM3. These three models simulate a substantial amount of precipitation during most of the day. In particular, rain-free periods[8] cover less than 8% of the time in CanAM4, 30% in CNRM-CM5 and 39% in MRI-CGCM3, compared to 89% in observations.

Despite the lack of organized convective systems in models and the differences in the rain distribution at the diurnal scale, models overall agree with observations on the JAS mean rate (Fig. 6). It can thus be argued that the climatological average arises from compensating errors similar to those stressed in Stephens et al. (2010): precipitation occurs approximately twice as often as in observations, but at rates far too weak.

2) Fine-scale properties of cloud cover

The diurnal cycle of cloud cover impacts the water cycle, but also the surface energy balance, through the surface incoming shortwave flux in particular. Bouniol et al. (2012) highlighted that all cloud types present a well-marked diurnal cycle in the Sahel (Fig. 18). Two peaks of convective cloud occurrence can be identified (around 0900 and 1500 UTC), consistently with the arrival of propagating convective systems and locally-initiated convection. Low-level clouds associated with the daytime growth of the boundary layer increase

[8]Rain-free periods are defined as precipitation intensity lower than 2.10^{-3} mm h^{-1}, since some models do not generate rain rates that exactly equal to zero.

between 0900 and 1600 UTC. The maximum in mid-level cloud cover occurs between 0300 and 0600 UTC. Cirrus cloud cover decreases between 1200 and 1500 UTC. The distribution of cloud fraction, also displayed in Fig. 18, highlights the distinct cloud fractions associated with each cloud type: low-level and cirrus clouds are relatively broken, while mid-level and convective clouds are associated with high cloud fractions.

Consistently with the diurnal cycle of precipitation, clouds associated with convection are shifted towards midday in CanAM4, CNRM-CM5, HadGEM2-A, IPSL-CM5A-LR and MPI-ESM-LR, which induces a too early minimum high-level cloud cover. It is generally followed by a strong occurrence of deep clouds resulting from condensates detrained from convective updraft and treated in most models as a passive stratiform cloud (Del Genio 2011). However the results are contrasted, as models overestimating rain frequency of occurrence are not necessarily those that overestimates the cloud frequency at high levels (e.g., CanAM4 and MRI-CGM3).

IPSL-CM5B-LR and MRI-CGCM3 show to some extent an improved timing of mid-level cloud occurrence, but with inaccurate frequencies of occurrence. The diurnal cycle of low-level clouds is properly represented in CNRM-CM5 and CanAM4 even if the growth of the boundary layer seems to be slightly underestimated. HadGEM2-A and MRI-CGCM3 have a very low occurrence of these clouds, and they appear much too early. MPI-ESM-LR misses this type of clouds. IPSL-CM5A-LR and IPSL-CM5B-LR also miss them at Niamey, due to an ITCZ located to much southward. Both models capture them more to the south, with however a too early triggering in IPSL-CM5A-LR.

The statistics of cloud fraction associated with the various cloud types are very different from one model to another. IPSL-CM5A-LR, IPSL-CM5B-LR and HadGEM2 simulate only broken clouds for deep and mid-level clouds, whereas only high cloud fraction values occur in MPI-ESM-LR. CNRM-CM5 has a bimodal distribution, but with an unphysical peak at 65% for the deep cloud fraction. Finally, CanAM4 and MRI-CGCM3 also present a bimodal structure, with weak cloud fraction values for low-level clouds and high cloud fraction values in the upper levels.

6. Summary and conclusions

In this paper, we present a comprehensive analysis of the representation of the West African monsoon in the recently available CMIP5 simulations of both present-day and future climates. The model behavior over the Sahel region is examined across a range of timescales, going from climate change projections, multi-decadal and interannual variability to the intraseasonal and diurnal fluctuations. A specific emphasis is put on the use of a comprehensive set of observational data now available (in particular AMMA and satellite data) to evaluate the WAM representation across those scales.

CMIP5 climate change projections in surface air temperature and precipitation are found to be very similar to those of CMIP3. A robust tendency to warming over the Sahel is noticed (about 4 K on average in the RCP8.5 scenario), larger by 10 to 50% compared to the global warming. As in CMIP3, the spread of model projections remains very large for both temperature and precipitation. 80% of models agree on a modest drying around 20% over the westernmost Sahel (15°W–5°W), while about 75% of models agree on an increase of precipitation over the Sahel between 0°and 30°E, with a large spread on the amplitude. This relatively high agreement might however involve the deficiencies that coupled models have in simulating the Atlantic SSTs (Vizy et al. 2013). Overall, the precipitation response tends to be lower than the observed decadal variability in the second half of the twentieth century. Five outliers[9] predict a rainfall increase greater than 70%, which cancels part of the Sahel warming during the summer monsoon. In contrast, two CMIP3 models predict a strong drying of the Sahel, around 40%. Further investigation on the rainfall response mechanisms in those models should help to assess their credibility. It should be noted that temperature changes also remain very uncertain and that their consequences might be as

[9] The term "outlier" indicates here models that simulate a rather different response to the main stream.

dramatic as those associated with precipitation.

CMIP5 coupled models still suffer of major SST biases in the equatorial Atlantic, which induce a systematic southward shift of the ITCZ during the summer in most models, when they are compared to their AMIP counterpart. The similarity between these biases in CMIP3 and CMIP5 appeals to revisit the current strategy in climate modeling research programs.

The ability of coupled models to simulate the multi-decadal and interannual variability is assessed with AMIP, historical and pre-industrial control runs. The decadal variability of the twentieth century is underestimated in most of the last two types of experiments. In AMIP simulations, most models capture the partial recovery of monsoon rainfall of the recent decades, consistently with the role of SSTs in forcing Sahel precipitation (Giannini et al. 2003; Biasutti et al. 2008). The AMIP time sequence is however too short to get rid of internal variability, and ensemble AMIP simulations should be useful for further analysis.

Because of these strong biases in coupled experiments, further evaluation is performed in SST-imposed CMIP5 simulations using the 10°W–10°E AMMA transect. Almost all of them capture the broad features of a monsoon, but with various degree of accuracy:

- The averaged Sahel rainfall exhibits a large spread (±50%).
- The dispersion in surface air temperature is large over the Sahel and Sahara, and the simulation of the Saharan heat low and monsoon latitudinal position appear to be linked. The representation of the radiative aerosol properties and surface albedo in this arid region may explain part of this spread.
- The meridional structure of cloud cover, and its radiative impact, are tough challenges for CMIP5 models. This leads to large biases in the surface energy balance, which are likely to feedback on the monsoon at larger scales.
- The annual cycle of temperature exhibits a wide dispersion. This points to the importance of physical processes in the seasonal dynamics of temperature, and questions

some conclusions that could be drawn from models about the climate sensitivity of the phase and amplitude of the temperature annual cycle over the Sahel.

- The intermittence of precipitation over West Africa is large and only a few models reproduce it and more broadly the main features of intraseasonal variability of convection there. Results from the GFDL-HIRAM models suggest that intraseasonal variability is improved with higher resolution but not necessarily the WAM mean state.

The fine-scale properties of rainfall and clouds are further evaluated at selected sites, for which high-frequency physical diagnostics were provided by some CMIP5 models. It appears that the wrong phasing of the diurnal cycle of precipitation remains an issue, even though some major improvements can be noticed in two models. However, most of the precipitation over the Sahel is provided by large mesoscale propagating systems, whose representation is still a challenge.

To summarize, even if most CMIP5 models capture many features of the west African monsoon, they have not reached yet a degree of maturity which directly makes them trustable to anticipate climate changes and their impacts, especially with regards to rainfall. Though encouraging progresses have been achieved, many systematic and robust biases of the coupled and atmospheric models have not improved from CMIP3 to CMIP5. This weakens our confidence in climate projection over West Africa, and even beyond over remote regions such as the Pacific (e.g., Ding et al. 2012). A large program aiming to address these systematic biases needs to be designed by the research community, under the umbrella of international programs. The observational datasets, acquired with AMMA and more recent programs such as FENNEC (Washington et al. 2012), should be a backbone of these efforts.

The results of the present study point to the need to separate as much as possible the issues related to slow and fast physical processes. Many systematic errors appear rapidly and could be addressed with numerous short-duration numerical experiments based on observed case studies and high resolution modeling results. An example of such an approach is the Transpose-AMIP protocol, which appears as a promising tool to understand the physics of systematic atmospheric model biases (Williams et al. 2012, and reference therein). The analysis of short-term initialized coupled simulations may also provide an interesting framework to better understand SST biases in the tropical Atlantic (Huang et al. 2007; Vannière et al. 2013). For issues related to slow physics, it is further necessary to distinguish those related to remote and regional mechanisms. Regional models and regionally nudged global models seem to be the best tool to separate them (Joly and Voldoire 2009; Pohl and Douville 2011). Large surface radiative biases in arid and semi-arid regions are a major issue in current simulations. They lead to departure from the observed radiative balance. The surface albedo and the representation of aerosols and their radiative properties request dedicated numerical sensitivity experiments with common protocols.

The present study not only focuses on the West African monsoon basic state in CMIP5 simulations (e.g., the precipitation seasonal amount), but also contributes to the evaluation of the rainfall distribution along the summer season (e.g., intraseasonal variability). The good representation of this rainfall distribution is crucial for the analysis of agricultural yields, biomass and water resources. There is a need to further evaluate the ability of current models to represent and predict rainfall properties at these short time (and space) scales, including the monsoon onset and retreat, as well as dry and wet spells.

Acknowledgments.

Based on a French initiative, AMMA was built by an international scientific group and is currently funded by a large number of agencies, especially from France, UK, US and Africa, and by an EU program. Detailed information on scientific coordination and funding is available on the AMMA International web site `http://www.amma-international.org`.

We wish particularly to thank the Principal Investigators who make the various AMMA-CATCH ground-based measurements data sets available to the AMMA data base: S. Galle, C. Lloyd, B. Cappelaere, F. Timouk and L. Kergoat for the surface radiation measurements, T. Vischel, M. Gosset, G. Quantin and E. Mougin for the rain gauge network measurements.

The Pirata buoy measurements were provided by TAO Project Office of NOAA/PMEL.

The Niamey AMF data were obtained from the Atmospheric Radiation Measurement (ARM) Program Archive of the US Department of Energy. CloudSat data were obtained from CIRA of Colorado State University. ICARE and NASA gave access to the CALIOP data. The SRB and CERES data were obtained from the NASA Langley Research Center Atmospheric Sciences Data Center. CMAP Precipitation and Interpolated OLR data were provided by the NOAA/OAR/ESRL PSD, Boulder, Colorado, USA, from their Web site at `http://www.esrl.noaa.gov/psd/`. The CRU dataset was provided by the British Atmospheric Data Centre (BADC), from their Web site at `http://badc.nerc.ac.uk`. The GPCP 1DD and TRMM 3B42 data were provided by the NASA/Goddard Space Flight Center's Mesoscale Atmospheric Processes Laboratory, which develops and computes the 1DD as a contribution to the GEWEX Global Precipitation Climatology Project and the 3B42 as a contribution to TRMM. The CFSR data were developed by NOAA's National Centers for Environmental Prediction (NCEP) and were obtained from the NOAA's National Operational Model Archive and Distribution System (NOMADS) which is maintained at NOAA's National Climatic Data Center (NCDC). The MERRA data were acquired from the Goddard Earth Sciences (GES) Data and Information Services Center (DISC, `http://disc.sci.gsfc.nasa.gov`). ERA-Interim data were obtained from the ECMWF Data Server.

We acknowledge the World Climate Research Programme's Working Group on Coupled Modelling, which is responsible for CMIP, and we thank the climate modeling groups (listed in Table 1 of this paper) for producing and making available their model output. For CMIP, the U.S. Department of Energy's Program for Climate Model Diagnosis and Intercomparison provides coordinating support and led development of software infrastructure in partnership with the Global Organization for Earth System Science Portals.

F. Favot and S. Tyteca are greatly acknowledged for their support. We also acknowledge the support of the IPSL data center CICLAD and the IPSL distribution platform

PRODIGUER for providing us access to their computing resources and data.

Finally, we acknowledge the thoughtful comments of Edward Vizy and one anonymous reviewer, which clearly helped to clarify and improve the manuscript.

R. Roehrig acknowledge financial support from the European Commission's 7th Framework Programme, under Grant Agreement n°282672, EMBRACE project. D. Bouniol and F. Guichard were financially supported by CNES and the EUCLIPSE project from the European Union, Seventh Framework Programme (FP7/2007–2013) under grant agreement n°244067. F. Guichard and F. Hourdin acknowledge financial support from the ESCAPE program (ANR-10-CEPL-005).

REFERENCES

Bao, X. and F. Zhang, 2012: Evaluation of NCEP/CFSR, NCEP/NCAR, ERA-Interim and ERA-40 reanalysis datasets against independent sounding observations over the Tibetan Plateau. *J. Climate*, **26**, 206–214, doi:10.1175/JCLI-D-12-00056.1.

Betts, A. and C. Jakob, 2002: Study of diurnal cycle of convective precipitation over Amazonia using a single column model. *J. Geophys. Res.*, **107 (D23)**, D23, doi: 10.1029/2002JD002264.

Biasutti, M. and A. Giannini, 2006: Robust Sahel drying in response to late 20th century forcings. *Geophys. Res. Lett.*, **33**, L11706, doi:10.1029/2006GL026067.

Biasutti, M., I. M. Held, A. H. Sobel, and A. Giannini, 2008: SST forcings and Sahel rainfall variability in simulations of the twentieth and twenty-first centuries. *J. Climate*, **21**, 3471–3486.

Bony, S., M. Webb, C. Bretherton, S. Klein, P. Siebesma, G. Tselioudis, and M. Zhang, 2011: CFMIP: towards a better evaluation and understanding of clouds and cloud feedbacks in CMIP5 models. *CLIVAR Exchanges No 56*, **16 (2)**, 20–24.

Boone, A. A., I. Poccard-Leclercq, Y. Xue, J. Feng, and P. de Rosnay, 2010: Evaluation of the WAMME model surface fluxes using results from de AMMA land-surface model intercomparison project. *Clim. Dyn.*, **35**, 127–142, doi:10.1007/s00382-009-0653-1.

Bouniol, D., F. Couvreux, P.-H. Kamsu-Tamo, M. Leplay, F. Guichard, F. Favot, and E. O'Connor, 2012: Diurnal and seaonal cycles of cloud occurrences, types and radiative impact over West Africa. *J. Appl. Meteor. Climatol.*, **51**, 534–553, doi:10.1175/JAMC-D-11-051.1.

Bouniol, D., J. Delanoë, C. Duroure, A. Protat, V. Giraud, and G. Penide, 2010: Microphysical characterisation of west African MCS anvils. *Quart. J. Roy. Meteor. Soc.*, **136 (s1)**, 323–344, doi:10.1002/qj557.

Chauvin, F., R. Roehrig, and J.-P. Lafore, 2010: Intraseasonal variability of the Saharan Heat Low and its link with mid-latitudes. *J. Climate*, **23**, 2544–2561.

Chikira, M. and M. Sugiyama, 2010: A cumulus parameterization with state-dependent entrainment rate. Part I: description and sensitivity to temperature and humidity profiles. *J. Atmos. Sci.*, **67**, 2171–2193.

Chou, C. and J. D. Neelin, 2003: Mechanisms limiting the northward extent of the nothern summer monsoons over North America, Asia, and Africa. *J. Climate*, **16**, 406–425.

Chou, C., J. D. Neelin, C.-A. Chen, and J.-Y. Tu, 2009: Evaluating the rich-get-recher mechanism in tropical precipitation change under global warming. *J. Climate*, **22**, 1982–2005.

Collins, W. J., et al., 2008: Evalution of the HadGEM2 model. Technical note 74, Meteorological Office Hadley Centre, Exeter, England. URL `http://www.metoffice.gov.uk/publications/HCTN/HCTN_74.pdf`.

Cook, K. H., 2008: Climate science: The mysteries of Sahel droughts. *Nat. Geosci.*, **1.**, 647–648.

Cook, K. H. and E. K. Vizy, 2006: Coupled model simulations of the West African monsoon system: twentieth- and twenty-first-century simulations. *J. Climate*, **19**, 3681–3703.

Del Genio, A. D., 2011: Representing the sensitivity of convective cloud systems to tropospheric humidity in general circulation models. *Surveys in Geophysics*, doi:10.1007/s10712-011-9148-9.

Depraetere, C., M. Gosse, S. Ploix, and H. Laurent, 2009: The organization and kinematics of tropical rainfall systems gournd tracked at mesoscale with gages: first results from the campaign 1999–2006 on the Upper Ouémé Valley (Benin). *J. Hydrol.*, **375 (1-2)**, 143–160, doi:10.1016/j.hydrol.2009.01.011.

Dhonneur, G., 1981: Les amas nuageux mobiles: principale composante de la métérologie du Sahel. *La Météorologie*, **27**, 75–82.

Ding, H., N. S. Keenlyside, and M. Latif, 2012: Impact of the Equatorial Atlantic on the El Niño Southern Oscillation. *Clim. Dyn.*, **38 (9)**, 1965–1972, doi:10.1007/s00382-011-1097-y.

Donner, L. J., et al., 2011: The dynamical core, physical paramterizations, and basic simulation characteristics of the atmospheric component of the GFDL glocabl coupled model CM3. *J. Climate*, **24**, 3484–3518.

Dufresne, J.-L., et al., 2012: Climate change projections using the IPSL-CM5 Earth system model: from CMIP3 to CMIP5. *Clim. Dyn.*, doi:10.1007/s00382-012-1636-1.

Emori, S., T. Nozawa, A. Numaguti, and I. Uno, 2001: Importance of cumulus parameterization for precipitation simulation over East Asia in June. *J. Meteor. Soc. Japan*, **79**, 939–947.

Fink, A. and A. Reiner, 2003: Spatio-temporal variability of the relation between African easterly waves and West African squall lines in 1998–1999. *J. Geophys. Res.*, **108 (D11)**, 4332, doi:10.1029/2002JD002816.

Fink, A. H., D. G. Vincent, and V. Emert, 2002: Rainfall types in the West African Sudanian zone during the summer monsoon 2002. *Mon. Wea. Rev.*, **134**, 2143–2164, doi:10.1175/MWR3182.1.

Gent, P. R., et al., 2011: The Community Climate System Model Version 4. *J. Climate*, **24 (19)**, 4973–4991.

Giannini, A., R. Saravanan, and P. Chang, 2003: Oceanic forcing of Sahel rainfall on interannual to interdecadal timescales. *Science*, **302**, 1027–1030.

Giorgetta, M. A., et al., 2012: The atmospheric general circulation model ECHAM6: model description. Tech. rep., Max Plank Institut für Meteorologie, Hamburg, Germany. URL `http://www.mpimet.mpg.de/en/science/models/echam.html`.

Grandpeix, J.-Y. and J.-P. Lafore, 2010: A density current parameterization coupled with Emanuel's convection scheme. Part I: the models. *J. Atmos. Sci.*, **67 (4)**, 881–897.

Guichard, F., L. Kergoat, E. Mougin, F. Timouk, F. Baup, P. Hiernaux, and F. Lavenu, 2009: Surface thermodynamics and radiative budget in the Sahelian Gourma: seasonal and diurnal cycles. *J. Hydrol.*, **375 (1-2)**, 161–177.

Guichard, F. et al., 2004: Modeling the diurnal cycle of deep precipitating convection over land with cloud-resolving models and single-column models. *Quart. J. Roy. Meteor. Soc.*, **130**, 3139–3172.

Hazeleger, W., et al., 2010: EC-Earth: a seamless Earth system prediction approach in action. *Bull. Amer. Meteor. Soc.*, **91**, 1357–1363, doi:10.1175/2010BAMS2877.1.

Held, I. M., T. L. Delworth, J. Lu, K. L. Findell, and T. R. Knutson, 2005: Simulation of Sahel drought in the 20th and 21th centuries. *Proc. Natl. Acad. Sci. U. S. A.*, **102**, 17 891–17 896.

Hoerling, M., J. Hurrell, J. Eischeid, and A. Phillips, 2006: Detection and attribution of twentieth-century northern and southern African rainfall change. *J. Climate*, **19**, 3989–4008.

Hourdin, F., et al., 2010: AMMA-Model Intercomparison Project. *Bull. Amer. Meteor. Soc.*, **91 (1)**, 95–104.

Hourdin, F., et al., 2012: LMDZ5B: the atmospheric component of the IPSL climate model with revisited parameterizations for clouds and convection. *Clim. Dyn.*, doi: 10.1007/s00382-012-1343-y.

Huang, B., Z.-Z. Hu, and B. Jha, 2007: Evoluation of model systematic errors in the Tropical Atlantic Basin from coupled climate hindcasts. *Clim. Dyn.*, **28**, 661–682, doi:10.1007/s00382-006-0223-8.

Huffman, G. J., R. F. Adler, M. M. Morrissey, D. T. Bolvin, S. Curtis, R. Joyce, B. McGavock, and J. Susskind, 2001: Global precipitation of one-degree daily resolution from multisatellite observations. *J. Hydrometeor.*, **2**, 36–50.

Huffman, G. J., D. T. Bolvin, E. J. Nelkin, D. B. Wolff, G. Gu, Y. Hong, K. P. Bowman, and E. F. Stocker, 2007: The TRMM Multisatellite Precipitation Analysis (TMPA): Quasi-global, multiyear, combined-sensor precipitation estimates at fine scales. *J. Hydrometeor.*, **8 (1)**, 38–55.

Janicot, S., F. Mounier, S. Gervois, B. Sultan, and G. Kiladis, 2010: The dynamics of the West African monsoon. Part V: The detection and role of the dominant modes of convectively coupled equatorial Rossby waves. *J. Climate*, **23**, 4005–4024.

Janicot, S., et al., 2011: Intraseasonal variability of the West African monsoon. *Atmos. Sci. Let.*, **12 (1)**, 58–66, doi:10.1002/asl.280.

Joly, M. and A. Voldoire, 2009: Influence of ENSO on the West African monsoon: temporal aspects and atmospheric processes. *J. Climate*, **22**, 3193–3210.

Jones, C. G., F. Giorgi, and G. Asrar, 2011: The Coordinated Regional Downscaling Experiment: CORDEX. An international downscaling link to CMIP5. *CLIVAR Exchanges No 56*, **16 (2)**, 34–400.

Kiladis, G. N., C. D. Thorncroft, and N. M. J. Hall, 2006: Three-dimensional structure and dynamics of African easterly waves. Part I: Obsevations. *J. Atmos. Sci.*, **63**, 2212–2230.

Kirkevåg, A., T. Iversen, O. Seland, J. B. Debernard, T. Storelvmo, and J. E. Kristjánsson, 2008: Aerosol-cloud-climate interactions in the climate model CAM-Oslo. *Tellus*, **60A**, 492–512.

Knippertz, P. and M. C. Todd, 2012: Mineral dust aerosols over the Sahara: meteorological controls on emission and transport and implications for modeling. *Rev. Geophys.*, **50**, RG1007, doi:10.1029/2011RG000362.

Kothe, S. and B. Ahrens, 2010: On the radiation budget in regional climate simulations of West Africa. *J. Geophys. Res.*, **115**, D23120, doi:10.1029/2010JD014331.

Lau, K. M., S. S. P. Shen, K.-M. Kim, and H. Wang, 2006: A multimodel study of the twentieth-century simulations of Sahel drought from the 1970s to 1990s. *J. Geophys. Res.*, **111**, D07111, doi:10.1029/2005JD006281.

Lavaysse, C., C. Flamant, S. Janicot, D. J. Parker, J.-P. Lafore, B. Sultan, and J. Pelon, 2009: Seasonal evolution of the West African heat low: a climatological perspective. *Clim. Dyn.*, **33 (2-3)**, 313–330, doi:10.1007/s00382-009-0553-4.

Le Lay, M. and S. Galle, 2005: Seasonal cycle and interannual variability of rainfall at hydrological scales. The West African monsoon in a Sudanese climate. *Hydrological Sciences Journal*, **50**, 3509–3524.

Lebel, T. and A. Ali, 2009: Recent trends in the Central and Western Sahel rainfall regime (1990–2007). *J. Hydrol.*, **375 (1–2)**, 52–64.

Lebel, T., et al., 2009: AMMA-CATCH studies in the Sahelian region of West-Africa: An overview. *J. Hydrol.*, **375 (1–2)**, 3–13, doi:10.1016.j.hydrol.2009.03.020.

Lebel, T., et al., 2010: The AMMA field campaigns: Multiscale and multidisciplinary observations in the West African region. *Quart. J. Roy. Meteor. Soc.*, **136 (s1)**, 8–33.

Liebmann, B. and C. A. Smith, 1996: Description of a complete (interpolated) outgoing longwave radiation dataset. *Bull. Amer. Meteor. Soc.*, **77**, 1275–1277.

Lin, J.-L. et al., 2006: Tropical intraseasonal variability in 14 IPCC AR4 climate models. Part I: Convective signals. *J. Climate*, **19**, 2665–2690.

Loeb, N. G., B. A. Wielicki, D. R. Doelling, G. L. Smith, D. F. Keyes, S. Kato, N. Manalo-Smith, and T. Wong, 2009: Towards optimal closure of the Earth's top-of-atmosphere radiation budget. *J. Climate*, **22**, 748–766, doi:10.1175/2008JCLI2637.1.

Mathon, V., H. Laurent, and T. Lebel, 2002: Mesoscale convective system rainfall in the Sahel. *J. Appl. Meteorol.*, **41**, 1081–1092.

Meehl, G. and Coauthors, 2007: Global Climate Projection. *Climate Change 2007: The Physical Science Basis. Contribution of Working Group I to the Fourth Assessment Report of the Intergovernmental Panel on Climate Change*, S. Solomon, D. Qin, M. Manning, Z. Chen, M. Marquis, K. B. Averyt, M. Tignor, and H. L. Miller, Eds., Cambridge University Press, Cambridge, United Kingdom and New York, NY, USA, 747–846.

Meehl, G. A., C. Covey, T. Delworth, M. Latif, B. McAvaney, J. F. B. Mitchell, R. J. Stouffer, and K. E. Taylor, 2007: The WCRP CMIP3 multimodel dataset: A new era in climate change research. *Bull. Amer. Meteor. Soc.*, **88**, 1383–1394.

Miller, M. A. and A. Slingo, 2007: The ARM Mobile Facility and its first international deployment: measuring flux divergence in West Africa. *Bull. Amer. Meteor. Soc.*, **88**, 1229–1244, doi:10.1175/BAMS-88-8-1229.

Mitchell, T. D. and P. D. Jones, 2005: An improved method of constructing a database of monthly climate observations and associated high-resolution grids. *Int. J. Climatol.*, **25 (6)**, 673–712, doi:10.1002/joc.1181.

Mizuta, R., et al., 2012: Climate simulations using MRI-AGCM3.2 with 20-km grid. *J. Meteor. Soc. Japan*, **90A**, 233–258.

Mounier, F. and S. Janicot, 2004: Evidence of two independant modes of convection at intraseasonal timescale in the West African summer monson. *Geophys. Res. Lett.*, **31**, L16116, doi:10.1029/2004GL020665.

Mounier, F., S. Janicot, and G. N. Kiladis, 2008: The West African monsoon dynamics. Part III: The quasi-biweekly zonal dipole. *J. Climate*, **21**, 1911–1928.

Neale, R. B., et al., 2010a: Description of the NCAR Community Atmospheric Model (CAM4.0). Technical note NCAR/TN-485+STR, National Center for Atmospheric Research, Boulder, Colorado, USA. URL `http://www.cesm.ucar.edu/models/ccsm4.0/cam/docs/description/cam4_desc.pdf`.

Neale, R. B., et al., 2010b: Description of the NCAR Community Atmospheric Model (CAM5.0). Technical note NCAR/TN-486+STR, National Center for Atmospheric Research, Boulder, Colorado, USA.

Nicholson, S., 1980: The nature of rainfall fluctuations in subtropical West Africa. *Mon. Wea. Rev.*, **108**, 473–487.

Nicholson, S. E., B. Some, and B. Kone, 2000: An analysis of recent rainfall conditions in West Africa, including the rainy seasons if the 1997 El Niño and the 1998 La Niña years. *J. Climate*, **13 (14)**, 2628–2640.

Nikulin, G., et al., 2012: Precipitation climatology in an esemble of CORDEX-Africa regional climate simulations. *J. Climate*, **25**, 6057–6078, doi:10.1175/JCLI-D-11-00375.1.

Paeth, H. and A. Hense, 2004: SST versus climate change signals in West African rainfall: 20th-century variations and future projections. *Climatic Change*, **65**, 179–208.

Pan, D.-M. and D. A. Randall, 1998: A cumulus parameterization with prognostic closure. *Quart. J. Roy. Meteor. Soc.*, **124**, 949–981.

Pohl, B. and H. Douville, 2011: Diagnosing GCM errors over West Africa using relaxation experiments. Part I: summer monsoon climatology and interannual variability. *Clim. Dyn.*, **37**, 1293–1312, doi:10.1007/s00382-010-0911-2.

Ramel, R., H. Gallée, and C. Messager, 2006: On the northward shift of the West African monsoon. *Clim. Dyn.*, **26 (4)**, 429–440, doi:10.1007/s00382-005-0093-5.

Redelsperger, J.-L., C. D. Thorncroft, A. Diedhiou, T. Lebel, D. J. Parker, and J. Polcher, 2006: African Monsoon Multidisciplinary Analysis: an international research project and field campaign. *Bull. Amer. Meteor. Soc.*, **87**, 1739–1746.

Richter, I. and S.-P. Xie, 2008: On the origin of equatorial Atlantic biases in coupled general circulation models. *Clim. Dyn.*, **31 (5)**, 587–598, doi:10.1007/s00382-008-0364-z.

Rickenbach, T., R. N. Ferreira, N. Guy, and E. Williams, 2009: Radar-observed squall line propagation and the diurnal cycle of convection in Niamey, Niger, during the 2006 African Monsoon and Multidisciplinary Analyses Intensive Observing Period. *J. Geophys. Res.*, **114**, D03107, doi:10.1029/2008JD010871.

Rienecker, M. M., et al., 2011: MERRA - NASA's Modern-Era Retrospective Analysis for Research and Applications. *J. Climate*, **24**, 3624–3648, doi:10.1175/JCLI-D-11-00015.1.

Rio, C. and F. Hourdin, 2008: A thermal plume model for convective boundary layer: representation of cumulus clouds. *J. Atmos. Sci.*, **65**, 407–425.

Rio, C., et al., 2012: Control of deep convection by sub-cloud lifting processes: the

ALP closure in the LMDZ5B general circulation model. *Clim. Dyn.*, doi:10.1007/s00382-012-1506-x.

Roehrig, R., 2010: Variabilité intrasainnière de la mousson africaine : Caractérisation et Modélisation (Intraseasonal variability of the West African monsoon : Characterization and modeling). Ph.D. thesis, Paris-Est University.

Roehrig, R., F. Chauvin, and J.-P. Lafore, 2011: 10-25-day intraseasonal variability of convection over the Sahel: a role of the Saharan heat low and midlatitudes. *J. Climate*, **24**, 5863–5878, doi:10.1175/2011JCLI3960.1.

Rotstayn, L., M. Collier, M. Dix, Y. Feng, H. Gordon, S. O'Farrell, I. Smith, and J. Syktus, 2010: Improved simulation of Australian climate and ENSO-related climate variability in a GCM with interactive aerosol treatment. *Int. J. Climatol*, **30 (7)**, 1067–1088, doi:10.1002/joc.1952.

Ruti, P. M. and A. Dell'Aquila, 2010: The twentieth century African easterly waves in reanalysis systems and IPCC simulations, from intra-seasonal to inter-annual variability. *Clim. Dyn.*, **35**, 1099–1117, doi:10.1007/s00382-010-0894-z.

Saha, S., et al., 2010: The NCEP climate forecast system reanalysis. *Bull. Amer. Meteor. Soc.*, **91**, 1015–1057, doi:10.1175/2010BAMS2001.1.

Sane, Y., et al., 2012: Analysis of the diurnal cycle of precipitation over Dakar using local rain-gauge data and a general circulation model. *Quart. J. Roy. Meteor. Soc.*, **138 (669)**, 2182–2195, doi:10.1002/qj.1932.

Simmons, A., S. Uppala, D. Dee, and S. Kobayashi, 2007: ERA-Interim: New ECMWF reanalysis products from 1989 onwards. *ECMWF Newsletter*, **110**.

Slingo, A., H. E. White, N. A. Bharmal, and G. J. Robinson, 2009: Overview of observations from the RADAGAST experiment in Niamey, Niger: 2. radiative fluxes and divergences. *J. Geophys. Res.*, **114**, D00E04, doi:10.1029/2008JD010497.

Slingo, J., 1980: A cloud parameterization scheme derived from GATE data for use with a numerical model. *Quart. J. Roy. Meteor. Soc.*, **106**, 747–770.

Stackhouse, P. W., Jr., S. K. Gupta, S. J. Cox, J. C. Mikovitz, T. Zhang, and L. M. Hinkelman, 2011: The NASA/GEWEX Surface Radiation Budget Release 3.0: 24.5-year dataset. *GEWEX News*, **21 (1)**, 10–12.

Stephens, G. L., et al., 2010: Dreary state of precipitation in global models. *J. Geophys. Res.*, **115**, D24211, doi:10.1029/2010JD014532.

Sultan, B., C. Baron, M. Dingkuhn, and S. Janicot, 2005: Agricultural impacts of large-scale variability of the West African monsoon. *Agricultural and Forest Meteorology*, **128**, 93–110.

Sultan, B. and S. Janicot, 2000: Abrupt shift of the ITCZ over West Africa and intra-seasonal variability. *Geophys. Res. Lett.*, **27**, 3353–3356.

Sultan, B. and S. Janicot, 2003: The West African monsoon dynamics. Part II: The "preonset" and "onset" of the summer monsoon. *J. Climate*, **16**, 3407–3427.

Taylor, K. E., R. J. Stouffer, and G. A. Meehl, 2012: An overview of CMIP5 and the experiment design. *Bull. Amer. Meteor. Soc.*, **93 (4)**, 485–498, doi:10.1175/BAMS-D-11-00094.1.

Thorncroft, C. D. and M. Blackburn, 1999: Maintenance of the African easterly jet. *Quart. J. Roy. Meteor. Soc.*, **125**, 763–786.

Thorncroft, C. D. and D. P. Rowell, 1998: Interannual variability of African wave activity in a general circulation model. *Int. J. Climatol.*, **18**, 1305–1323.

Timouk, F., L. Kergoat, E. Mougin, C. Lloyd, E. Ceschia, P. de Rosnay, P. Hiernaux, and V. Demarez, 2009: Response of sensible heat flux to water regime and vegetation development in a central Sahelian landscape. *J. Hydrol.*, **375**, 178–189.

Tippett, M. and A. Giannini, 2006: Potentially predictable components of African summer rainfall in a SST-forced GCM simulation. *J. Climate*, **19**, 3133–3144.

Vannière, B., E. Guilyardi, G. Madec, Doblas-Reyes, F. J., and S. Woolnough, 2013: Using seasonal hindcasts to understand the origin of the equatorical cold tongue bias in CGCMs and its impact on ENSO. *Clim. Dyn.*, **40 (3–4)**, 963–981, doi:10.1007/s00382-012-1429-6.

Vizy, E. K., K. H. Cook, J. Crétat, and N. Neupane, 2013: Projections of a wetter Sahel in the 21st century from global and regional models. *Submitted to J. Climate.*

Voldoire, A., et al., 2012: The CNRM-CM5.1 global climate model: description and basic evaluation. *Clim. Dyn.*, doi:10.1007/s00382-011-1259-y.

Volodin, E. M., N. A. Diansky, and A. V. Gusev, 2010: Simulating present-day climate with the INMCM4.0 coupled model of the atmospheric and oceanic general circulations. *Atmospheric and Oceani Physics*, **46**, 414–431.

Waliser, D. E., J.-L. Li, T. L'Ecuyer, and W.-T. Chen, 2011: The impact of precipitating ice and snow on the radiation balance in global climate models. *Geophys. Res. Lett.*, **38**, L06802, doi:10.1029/2010GL046478.

Wang, W., P. Xie, S.-H. Yoo, Y. Xue, A. Kumar, and X. Wu, 2011: An asseesment of the surface climate in the NCEP climate forecast system reanalysis. *Clim. Dyn.*, **37 (7)**, 1601–1620, doi:10.1007/s00382-010-0935-7.

Ward, M. N., 1998: Diagnosis and short-lead prediction of summer rainfall in tropical North Africa at interannual and multidecadal timescales. *J. Climate*, **11**, 3167–3191.

Washington, R., et al., 2012: Fennec: the Saharan climate system. *4th international AMMA Conference, 2-6 July 2012, Toulouse, France.*

Watanabe, M., et al., 2010: Improved climate simulation by MIROC5: mean states, variability, and climate sensitivity. *J. Climate*, **23**, 6312–6335, doi:10.1175/2010JCLI3679.1.

Wielicki, B. A., B. R. Barkstrom, E. F. Harrison, R. B. Lee III, G. L. Smith, and J. E. Cooper, 1996: Clouds and the Earth's Radiant Energy System (CERES): An Earth observing system experiment. *Bull. Amer. Meteor. Soc.*, **77**, 853–868.

Williams, K. D., et al., 2012: The Transpose-AMIP II experiment and its application to the understanding of Southern Ocean cloud biases in climate models. *J. Climate*, doi: 10.1175/JCLI-D-12-00429.1.

Wu, T., et al., 2010: The Beijing Climate Center for Atmospheric General Circulation Model (BCC-AGCM2.0.1: description and its performance for the present-day climate. *Clim. Dyn.*, **34**, 123–147.

Xie, P. and P. A. Arkin, 1997: Global precipitation: a 17-year monthly analysis based on gauge observation, satellite estimates, and numerical model outputs. *Bull. Amer. Meteor. Soc.*, **78**, 2539–2558.

Xue, Y., et al., 2010: Intercomparison and analyses of the climatology of the West African Monsoon in the West AFrican Monsoon Modeling and Evaluation project (WAMME) first model intercomparison experiment. *Clim. Dyn.*, **35**, 3–28, doi:10.1007/s00382-010-0778-2.

Yang, S., K.-S. Kuo, and E. A. Smith, 2008: Persistent nature of secondary diurnal modes of precipitation over oceanic and continental regimes. *J. Climate*, **21 (16)**, 4115–4131.

Yokimoto, S., et al., 2011: Meteorological Research Institue-Earth System Model v1 (MRI-ESM1) - Model Description. Technical report 64, Meteorological Research Institute, Japan.

List of Tables

1 CMIP5 simulations used in the present study. 45

2 Characteristics of AMIP simulation models used in the present study. 46

3 Observational datasets. 47

Table 1. CMIP5 simulations used in the present study.

Centers	Models	Simulations
BCC (China)	BCC-CSM1.1	amip*, hist, rcp4.5, rcp8.5, picontrol
	BCC-CSM1.1(m)	hist, rcp4.5, rcp8.5
CCCma (Canada)	CanAM4	amip*†
	CanCM4	hist
	CanESM2	hist, rcp4.5
CMCC (Italy)	CMCC-CM	amip*, hist, rcp4.5, rcp8.5, picontrol
	CMCC-CMS	hist, rcp4.5, rcp8.5
	CMCC-CESM	hist, rcp8.5
CNRM-CERFACS (France)	CNRM-CM5	amip*†, hist, rcp4.5, rcp8.5, picontrol
CSIRO-BOM (Australia)	ACCESS1.0	amip, hist, rcp4.5, rcp8.5, picontrol
	ACCESS1.3	amip, hist, rcp4.5, rcp8.5, picontrol
CSIRO-QCCE (Australia)	CSIRO-Mk3.6.0	amip*, hist, rcp4.5, rcp8.5, picontrol
FIO (China)	FIO-ESM	hist, rcp4.5, rcp8.5
GCESS (China)	BNU-ESM	amip*, hist, rcp8.5, picontrol
ICHEC	EC-EARTH	amip*, hist, picontrol
INM (Russia)	INM-CM4	amip*, hist, rcp4.5, rcp8.5, picontrol
IPSL (France)	IPSL-CM5A-LR	amip*†, hist, rcp4.5, rcp8.5, picontrol
	IPSL-CM5A-MR	amip*, hist, rcp4.5, rcp8.5, picontrol
	IPSL-CM5B-LR	amip*†, hist, rcp4.5, rcp8.5, picontrol
LASG-CESS (China)	FGOALS-g2	amip*, hist, rcp4.5, rcp8.5, picontrol
LASG-IAP (China)	FGOALS-s2	amip*, hist, rcp4.5, rcp8.5, picontrol
MIROC (Japan)	MIROC4h	hist
	MIROC5	amip*, hist, rcp4.5, rcp8.5, picontrol
	MIROC-ESM	hist, rcp4.5, rcp8.5
	MIROC-ESM-CHEM	hist, rcp4.5, rcp8.5
MOHC (England)	HadCM3	hist
	HadGEM2-A	amip*†
	HadGEM2-CC	hist, rcp4.5, rcp8.5
	HadGEM2-ES	hist, rcp4.5, rcp8.5
MPI-M (Germany)	MPI-ESM-LR	amip*†, hist, rcp4.5, rcp8.5, picontrol
	MPI-ESM-MR	amip*, hist, rcp4.5, rcp8.5, picontrol
	MPI-ESM-P	hist
MRI (Japan)	MRI-AGCM3.2H	amip*
	MRI-AGCM3.2S	amip*
	MRI-CGCM3	amip*†, hist, rcp4.5, rcp8.5, picontrol
NASA-GISS (USA)	GISS-E2-H	hist, rcp4.5, rcp8.5
	GISS-E2-R	amip, hist, rcp4.5, rcp8.5, picontrol
	GISS-E2-H-CC	hist, rcp4.5
	GISS-E2-R-CC	hist, rcp4.5
NCAR (USA)	CCSM4	amip, hist, rcp8.5, picontrol
NCC (Norway)	NorESM1-M	amip*, hist, rcp4.5, rcp8.5, picontrol
	NorESM1-ME	hist, rcp4.5, rcp8.5
NIMR-KMA (South Korea)	HadGEM2-AO	hist, rcp4.5, rcp8.5
NOAA-GFDL (USA)	GFDL-CM2p1	hist
	GFDL-CM3	hist, rcp4.5, rcp8.5
	GFDL-ESM2G	hist, rcp4.5, rcp8.5
	GFDL-ESM2M	hist, rcp4.5, rcp8.5
	GFDL-HIRAM-C180	amip*
	GFDL-HIRAM-C360	amip*
NSF-DOE-NCAR (USA)	CESM1(BGC)	hist, rcp4.5, rcp8.5
	CESM1(CAM5)	amip, hist, rcp4.5, rcp8.5, picontrol
	CESM1(FASTCHEM)	hist
	CESM1(WACCM)	hist

* Daily outputs are available for these simulations.

† High-frequency output are used at selected sites.

TABLE 3. Observational datasets.

Variables	Dataset	References	Resolution	Frequency	Period covered
Rainfall	CRU version 3.1	Mitchell and Jones (2005)	0.5°x0.5°	monthly	1901–2008
	CMAP	Xie and Arkin (1997)	2.5°x2.5°	monthly	1979–2008
	GPCP	Huffman et al. (2001)	1°x1°	daily	1997–2008
	TRMM-3B42	Huffman et al. (2007)	0.25°x0.25°	daily	1998–2008
	Ouémé rain gauges (2°E-9.5°N)	Le Lay and Galle (2005); Depraetere et al. (2009)	site[a]	5/30 minutes	1999–2011
	Niamey rain gauges (2.2°E-13.5°N)	Lebel et al. (2010)	site[a]	5/30 minutes	1990–2011
Convection	NOAA OLR	Liebmann and Smith (1996)	2.5°x2.5°	daily	1979–2008
Clouds	CloudSat/CALIPSO	Bouniol et al. (2012)	AMMA transect[b]	monthly	2006–2010
	ARM Mobile Facility (AMF)	Miller and Slingo (2007); Bouniol et al. (2012)	Niamey site	30 minutes	2006
Radiation	CERES-EBAF[c] Edition 2.6	Wielicki et al. (1996); Loeb et al. (2009)	1°x1°	monthly	2000–2010
	NASA/GEWEX SRB release 3.0 (pr/qc)[d]	Stackhouse et al. (2011)	1°x1°	monthly	1983–2007
	Transect sites[e]	Lebel et al. (2009); http://www.amma.catch.org	sites	JAS average	
2-m temperature	CRU version 3.1	Mitchell and Jones (2005)	0.5°x0.5°	monthly	1979–2008
	NCEP CFSR	Saha et al. (2010)	1°x1°	monthly/daily	1979–2008
	NASA-MERRA	Rienecker et al. (2011)	1°x1°	monthly/daily	1979–2008
	ERA-Interim	Simmons et al. (2007)	0.75°x0.75°	monthly/daily	1979–2008

[a] The number and density of gauges vary from year to year. To match the 30-min model output resolutions extracted at these selected sites, and not oversample any particular region, the data were re-sampled and spatially homogenized in 0.2°x0.2° domain within 2°x2° area around both sites.
[b] Each satellite track within a 10°W-10°E domain is assumed representative of the Greenwich latitude, leading to at least two sampling per day along this transect.
[c] The Clouds and Earth's Radiant Energy System (CERES) Energy Balanced and Filled (EBAF) Edition 2.6 product consists of top-of-atmosphere and surface radiative fluxes (http://ceres.larc.nasa.gov).
[d] The NASA/GEWEX Surface Radiation Budget (SRB) consists of top-of-atmosphere and surface radiative fluxes. Two sets of surface radiative flux estimations are available, based on different algorithms, known as primary (SRB3pr) and Langley parameterized algorithms (SRB3qc). More information on these two datasets are available at http://gewex-srb.larc.nasa.gov/index.php.
[e] Bamba (17.1°N-1.4°E, 2004–2007), Agoufou (15.34°N-1.48°E, 2002–2008), Wankama (13.67°N-2.65°E, 2005–2006), Bira (9.82°N-1.71°E, 2006), Naholou (9.73°N-1.60°E, 2006) and PIRATA Buoy (0°-0°, 2006, only incoming shortwave at surface).

List of Figures

1 a) Climate projections of 2-meter temperature (colors in K) plotted as the difference between the periods 2071–2100 and 1971–2000 for the JAS season, for the CMIP3 SRES A2 ensemble mean. The CMIP3 inter-model standard deviation is indicated in contours, with one contour every 0.2 K, beginning at 1.0 K. b) Same as a) but for precipitation (in mm day^{-1}). The standard deviation is indicated in contours, with one contour every 0.3 mm day^{-1}, beginning at 1.0 mm day^{-1}. c) Percentage of models of the CMIP3 ensemble that agree on the sign of the CMIP3 ensemble mean precipitation changes. d), e), and f) same as a), b) and c) respectively, but for the CMIP5 RCP8.5 model ensemble. 54

2 a) Climate projections of precipitation (in %) plotted against those of 2-meter temperature (in K) averaged over a westernmost Sahel domain [10°N-18°N, 15°W-5°W], indicated on Fig. 1.a. The differences are computed between the periods 2071–2100 and 1971–2000, for the JAS season, for CMIP3 SRESA2 scenario and for CMIP5 RCP4.5 and RCP8.5 scenarios. b) Same as a), but for a eastern West Sahel domain [10°N-18°N, 0°-10°E]. c) Same as a) but for a central/eastern Sahel domain [10°N-18°N, 10°E-35°E]. d) Climate projections of global 2-meter temperature plotted against those of 2-meter temperature averaged over a Sahel domain [10°N-18°N, 15°W-35°E]. Open markers indicate projections for which precipitation change is greater than 25% over the whole Sahel domain. e) Same as d), but for the MAM season. 55

3 a) Time evolution of raw (thin line with dots) precipitation in mm day^{-1} averaged over [10°N-18°N, 0°-10°E] and of its decadal component $\overline{P}^9$ (thick solid line), computed as the 9-year running mean of the raw index. CRU data is indicated by the thick black line and CMAP by the thin black line. b) Precipitation difference (in %) between the 9-year periods 2000–2008 and 1979–1987 for AMIP simulations (dots), and standard deviation of $\overline{P}^9$ in historical (open squares) and pre-industrial control (grey filled squares) experiments. The standard deviations (in %) are computed on the full period (1850-2008) for historical simulations and on the available length for pre-industrial simulations, which ranges from 250 to 1000 years depending on the model. The standard deviation has been normalized by the mean $\overline{P}^9$. For observations, the square corresponds to the normalized standard deviation of CRU $\overline{P}^9$ while the two black circles correspond to the precipitation difference (in %) between the periods 2000–2008 and 1979-1987 in the CRU and CMAP observations. c) Standard deviation of interannual fluctuation $\delta P = P - \overline{P}^9$ as a fraction of the mean precipitation (in %), in pre-industrial control (grey filled squares) and historical (open squares) experiments. 56

4 Difference between historical and AMIP simulations for precipitation (shaded, mm day^{-1}) and 2-meter temperature (one contour every 1 K, the zero contour being omitted), averaged over the JAS seasons of the 1979–2008 period. The CMIP3 and CMIP5 ensemble means are shown in the bottom row, as well as the CMIP5 ensemble mean biases of historical and AMIP simulations against the CRU datasets. 57

5 Scatterplot of the ITCZ position against the meridional temperature gradient between the Gulf of Guinea and the Sahara desert. The ITCZ latitude corresponds to the JAS position of maximum precipitation averaged over 10°W-10°E. The JAS temperature gradient is computed as the difference between the domains [20°N-30°N, 10°W-10°E] and [5°S-5°N, 10°W-10°E]. 58

6 Precipitation (in mm day^{-1}) averaged over 10°W-10°E, for the JAS period of the years 1979-2008 for CMIP5 simulations, and 1997-2008 for GPCP, 1998-2008 for TRMM, 1979–2008 for CRU and 1979–2008 for CMAP datasets. Each dataset is displayed using its own horizontal resolution. The left (right) panel corresponds to the warmer (colder) models over the Sahara [20°N–30°N, 10°W–10°E]. 59

7 2-meter temperature (in K) averaged over 10°W-10°E, for the JAS period of the years 1979-2008 for CMIP5 simulations, reanalyses and CRU. Each dataset is displayed using its own horizontal resolution. The left (right) panel corresponds to the warmer (colder) models over the Sahara [20°N–30°N, 10°W–10°E]. 60

8 Latitude-height diagrams of the cloud fraction averaged between 10°W-10°E, for the period JAS of the years 2006-2010 for the CloudSat-CALIPSO data set and 1979-2008 for the models. Models are organized from the warmest one over the Sahara [20°N–30°N, 10°W–10°E] (top left after the observation panel) to the coldest one (bottom right). 61

9 a) and b) Cloud radiative effect (in W m^{-2}) at the top of the atmosphere in the SW (negative values) and LW (positive values) bands, averaged over 10°W-10°E, for the JAS period of the years 1979-2008. The left (right) panel corresponds to warmer (colder) models over the Sahara [20°N–30°N, 10°W–10°E]. c) and d) As in a) and b) respectively, but for the net CRE at the top of the atmosphere. 62

10 a) and b) Downward shortwave radiative flux at the surface (in W m^{-2}), averaged over 10°W-10°E, for the JAS period of the years 1979-2008. The left (right) panel corresponds to warmer (colder) models over the Sahara [20°N–30°N, 10°W–10°E]. Mean fluxes for the sites along the transect (Table 3) together with their yearly minimum and maximum values are indicated. c) and d) As in a) and b) respectively, but for the downward longwave radiative flux at the surface. 63

11 a) Scatterplot of the downward longwave radiative flux at the surface (in W m^{-2}) against the 2-meter temperature (in K). Both variables are averaged over [20°N-30°N, 10°W-10°E], for the JAS period of the years 1979-2008. A linear regression was performed and its coefficient of determination is indicated in the top-left corner. b) As in a), but for the downward shortwave radiative flux at the surface against the 2-meter temperature. Note that the linear regression was performed without the CNRM-CM5 data. c) as in b) but for the downward longwave radiative flux at the surface against the downward shortwave radiative flux at the surface (in W m^{-2}). The black square with error bars indicates the mean obtained from observational datasets, i.e. SRB3pr, SRB3qc and CERES-EBAF for radiative fluxes, and ERAI, MERRA and CFSR for the 2-meter temperature. The warmer (colder) models are indicated with dots (filled square). 64

12 Annual cycle of precipitation (in mm day^{-1}) averaged over 10°W-10°E. A 10-day running mean was performed on each dataset. Models are organized from the warmest one over the Sahara [20°N–30°N, 10°W–10°E] (top left after the observation panel) to the coldest one (bottom right). 65

13 Annual cycle of 2-meter temperature (in K) averaged over 10°W-10°E. Models are organized from the warmest one over the Sahara [20°N–30°N, 10°W–10°E] (top left after the observation panel) to the coldest one (bottom right). 66

14 Variance of OLR in the 1-90-day band, in W^2 m^{-4} for the JAS periods from 1979 to 2008. Daily OLR of CMIP5 models was regridded on the NOAA OLR grid (2.5°x2.5°), before computing filtered anomalies and their variance. 67

15 a) Variance of OLR in the 1-90-day band averaged over the domain [5°N-20°N, 10°W-10°E], and for the JAS periods from 1979 to 2008. Values are normalized by the NOAA OLR variance. b) Distribution of the OLR intraseasonal variance (in %) across the 1-3-day (grey bars), 3-10-day (white bars) and 10-90-day (black bars) bands. 68

16 a) Autocorrelation of a) JAS and b) DJF 1-90-day filtered precipitation at a 1-day lag for the GPCP daily dataset. Only grid-point where mean precipitation is greater than 1 mm day^{-1} are considered. c) Autocorrelation of 1-90-day filtered precipitation at a 1-day lag for GPCP and CMIP5 models, averaged over the domain [5°N-15°N,10°W-10°E]. Autocorrelation is computed for each JAS season of the period 1997-2008 for GPCP and 1979–2008 for CMIP5 model, and then averaged over all years. CMIP5 models and the GPCP dataset were regridded on the NOAA OLR grid before any computation. 69

17 Mean August diurnal cycle of precipitation intensity distribution (including null value). 1979-2008 is the period used for the models, 1999–2011 for the Ouémé site (2°E-9.5°N) and 1989–2011 for the Niamey site (2.2°E-13.5°N). The distribution is based on 30-min samples. The mean diurnal cycle of rainfall intensity is superimposed with the black line. Superimposed dashed lines also indicates the diurnal cycle of precipitation intensity distribution, but using 3-hourly samples for comparison with the CNRM-CM5 model. 70

18 As in Fig. 17 but for the August diurnal cycle of the cloud frequency of occurrence derived at the Niamey site (2.2°E-13.5°N). Observations comes from the AMF data acquired in 2006. The period 1979-2008 is used for the models. The vertical distribution of the cloud fraction is indicated on the right sub-panels. It is normalized at each level by the total cloud frequency of occurrence which is superimposed with the dashed line. 71

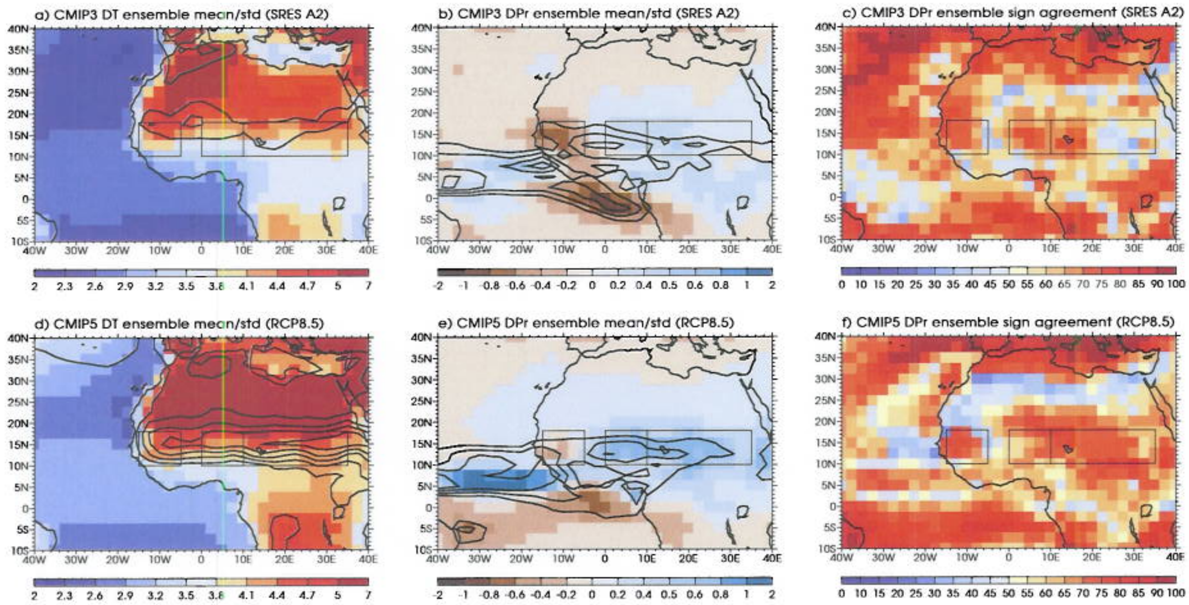

FIG. 1. a) Climate projections of 2-meter temperature (colors in K) plotted as the difference between the periods 2071–2100 and 1971–2000 for the JAS season, for the CMIP3 SRES A2 ensemble mean. The CMIP3 inter-model standard deviation is indicated in contours, with one contour every 0.2 K, beginning at 1.0 K. b) Same as a) but for precipitation (in mm day^{-1}). The standard deviation is indicated in contours, with one contour every 0.3 mm day^{-1}, beginning at 1.0 mm day^{-1}. c) Percentage of models of the CMIP3 ensemble that agree on the sign of the CMIP3 ensemble mean precipitation changes. d), e), and f) same as a), b) and c) respectively, but for the CMIP5 RCP8.5 model ensemble.

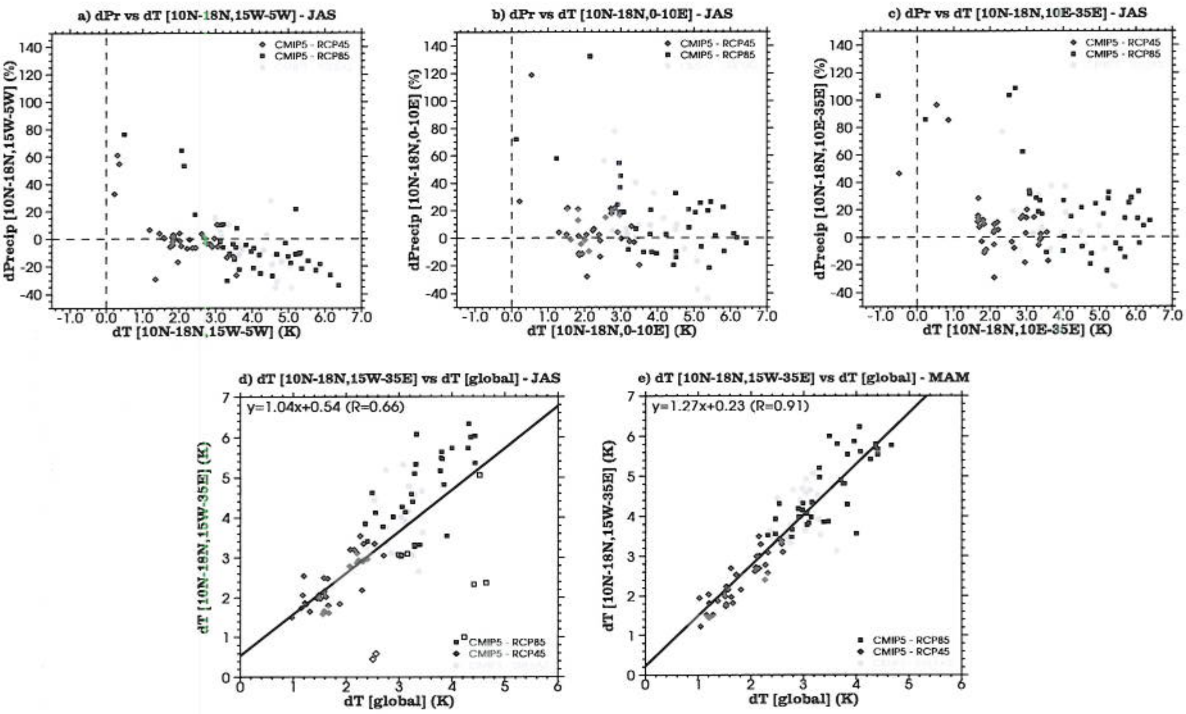

FIG. 2. a) Climate projections of precipitation (in %) plotted against those of 2-meter temperature (in K) averaged over a westernmost Sahel domain [10°N-18°N, 15°W-5°W], indicated on Fig. 1.a. The differences are computed between the periods 2071–2100 and 1971–2000, for the JAS season, for CMIP3 SRESA2 scenario and for CMIP5 RCP4.5 and RCP8.5 scenarios. b) Same as a), but for a eastern West Sahel domain [10°N-18°N, 0°-10°E]. c) Same as a) but for a central/eastern Sahel domain [10°N-18°N, 10°E-35°E]. d) Climate projections of global 2-meter temperature plotted against those of 2-meter temperature averaged over a Sahel domain [10°N-18°N, 15°W-35°E]. Open markers indicate projections for which precipitation change is greater than 25% over the whole Sahel domain. e) Same as d), but for the MAM season.

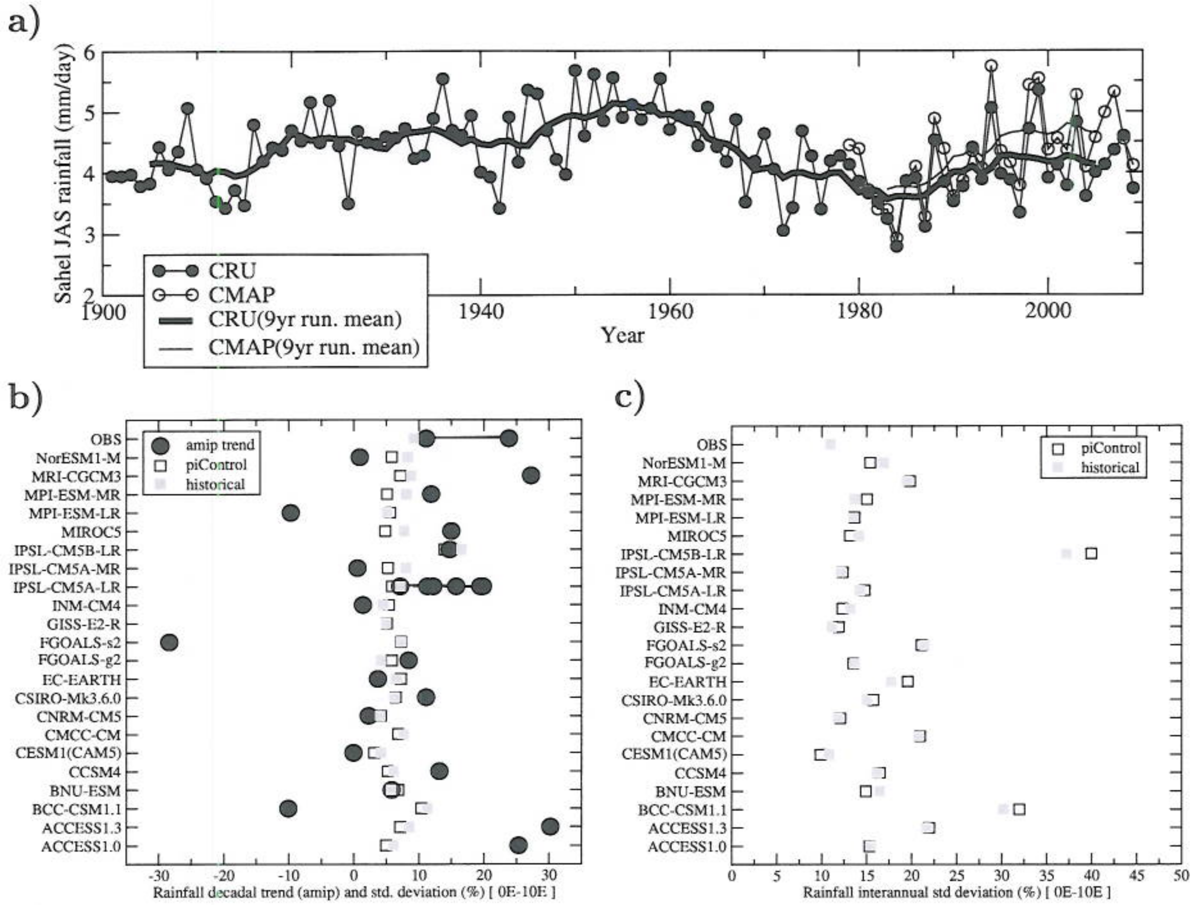

FIG. 3. a) Time evolution of raw (thin line with dots) precipitation in mm day^{-1} averaged over [10°N-18°N, 0°-10°E] and of its decadal component $\overline{P}^9$ (thick solid line), computed as the 9-year running mean of the raw index. CRU data is indicated by the thick black line and CMAP by the thin black line. b) Precipitation difference (in %) between the 9-year periods 2000–2008 and 1979–1987 for AMIP simulations (dots), and standard deviation of $\overline{P}^9$ in historical (open squares) and pre-industrial control (grey filled squares) experiments. The standard deviations (in %) are computed on the full period (1850-2008) for historical simulations and on the available length for pre-industrial simulations, which ranges from 250 to 1000 years depending on the model. The standard deviation has been normalized by the mean $\overline{P}^9$. For observations, the square corresponds to the normalized standard deviation of CRU $\overline{P}^9$ while the two black circles correspond to the precipitation difference (in %) between the periods 2000–2008 and 1979-1987 in the CRU and CMAP observations. c) Standard deviation of interannual fluctuation $\delta P = P - \overline{P}^9$ as a fraction of the mean precipitation (in %), in pre-industrial control (grey filled squares) and historical (open squares) experiments.

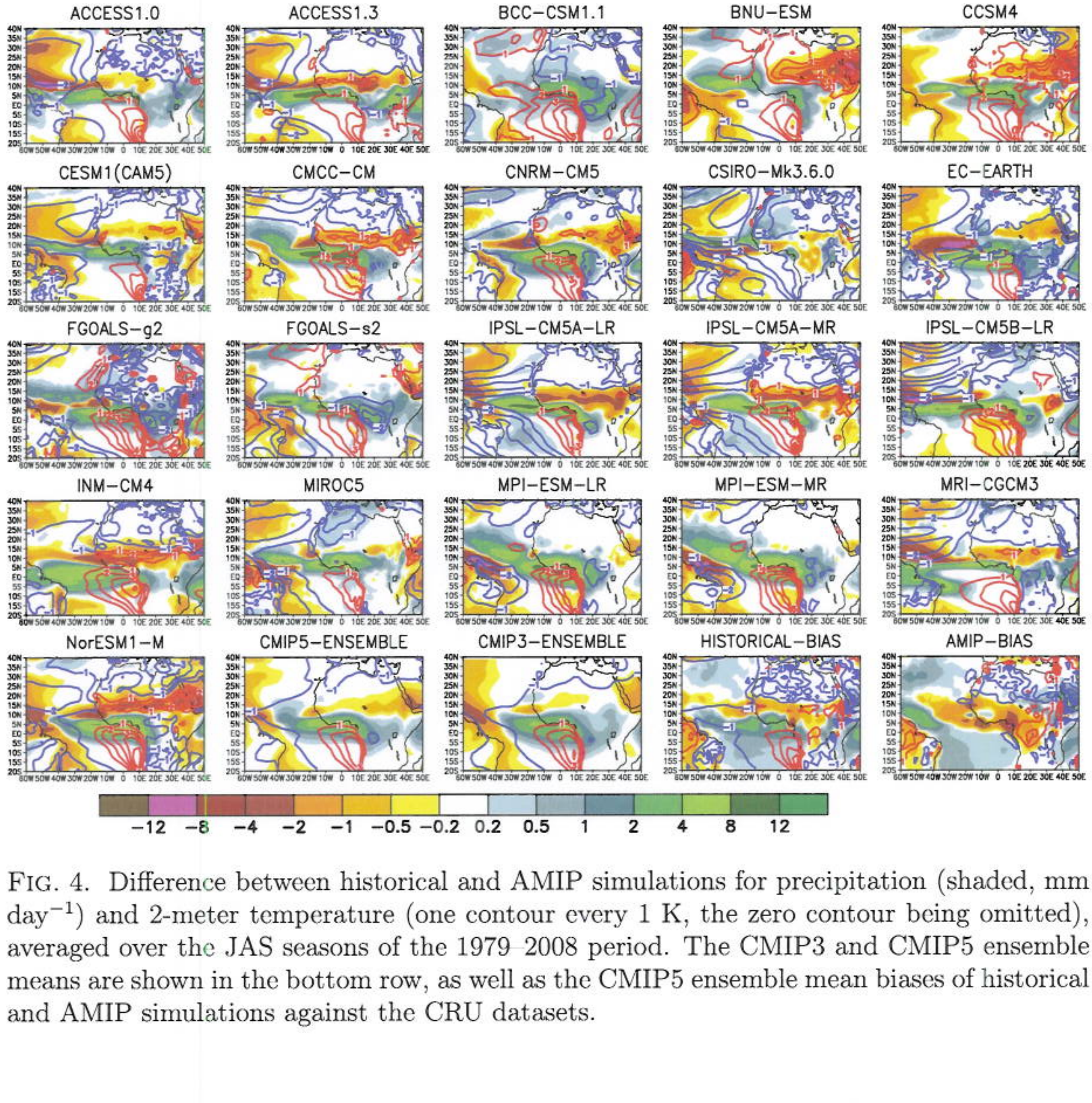

FIG. 4. Difference between historical and AMIP simulations for precipitation (shaded, mm day^{-1}) and 2-meter temperature (one contour every 1 K, the zero contour being omitted), averaged over the JAS seasons of the 1979–2008 period. The CMIP3 and CMIP5 ensemble means are shown in the bottom row, as well as the CMIP5 ensemble mean biases of historical and AMIP simulations against the CRU datasets.

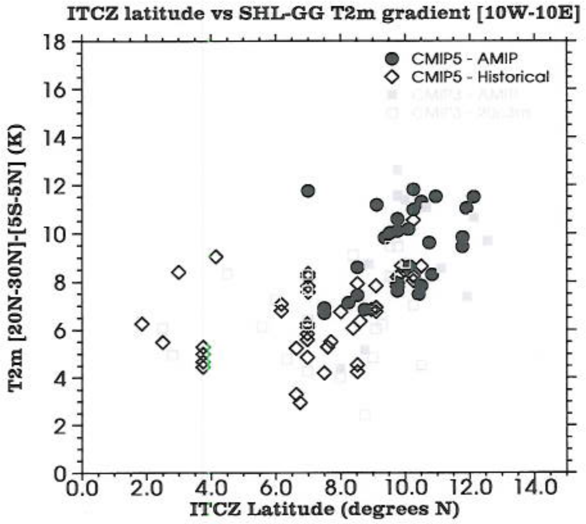

FIG. 5. Scatterplot of the ITCZ position against the meridional temperature gradient between the Gulf of Guinea and the Sahara desert. The ITCZ latitude corresponds to the JAS position of maximum precipitation averaged over 10°W-10°E. The JAS temperature gradient is computed as the difference between the domains [20°N-30°N, 10°W-10°E] and [5°S-5°N, 10°W-10°E].

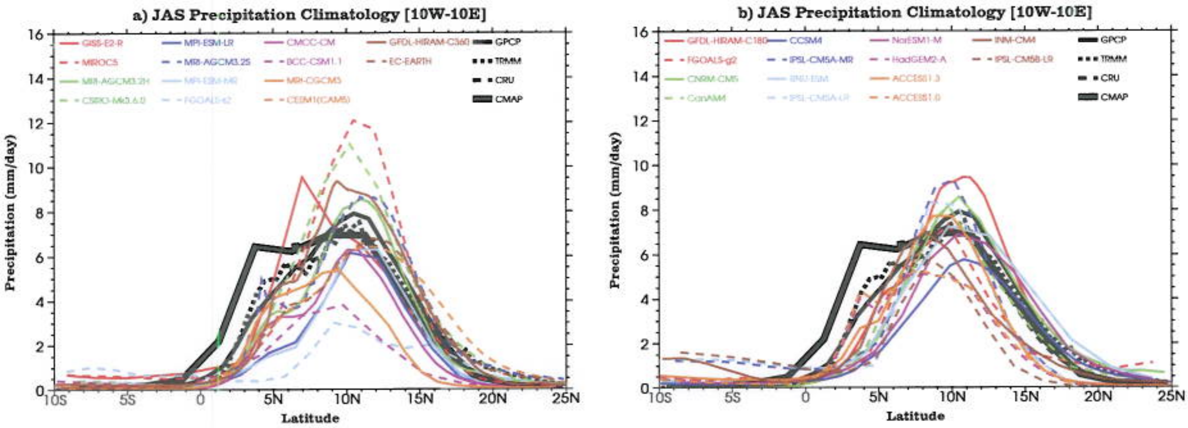

FIG. 6. Precipitation (in mm day^{-1}) averaged over 10°W-10°E, for the JAS period of the years 1979-2008 for CMIP5 simulations, and 1997-2008 for GPCP, 1998-2008 for TRMM, 1979–2008 for CRU and 1979–2008 for CMAP datasets. Each dataset is displayed using its own horizontal resolution. The left (right) panel corresponds to the warmer (colder) models over the Sahara [20°N–30°N, 10°W–10°E].

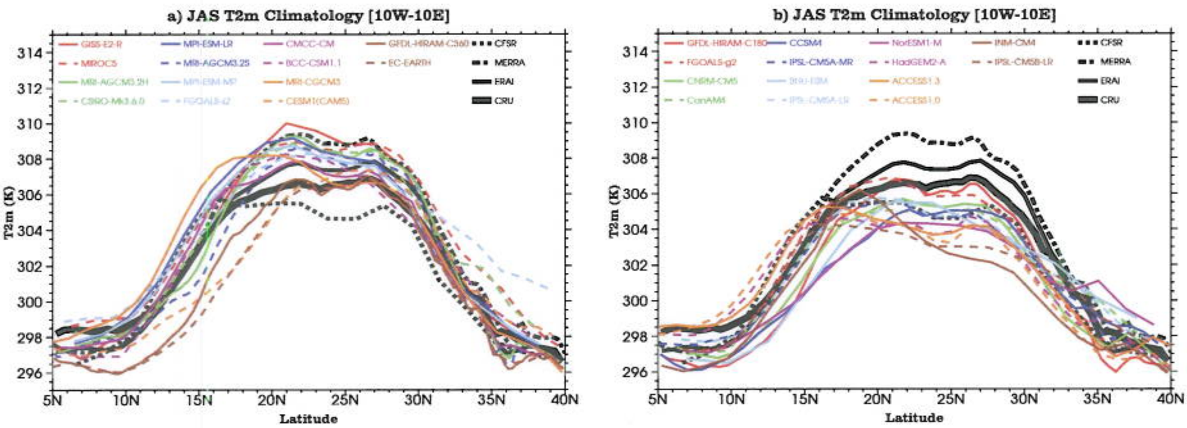

FIG. 7. 2-meter temperature (in K) averaged over 10°W-10°E, for the JAS period of the years 1979-2008 for CMIP5 simulations, reanalyses and CRU. Each dataset is displayed using its own horizontal resolution. The left (right) panel corresponds to the warmer (colder) models over the Sahara [20°N–30°N, 10°W–10°E].

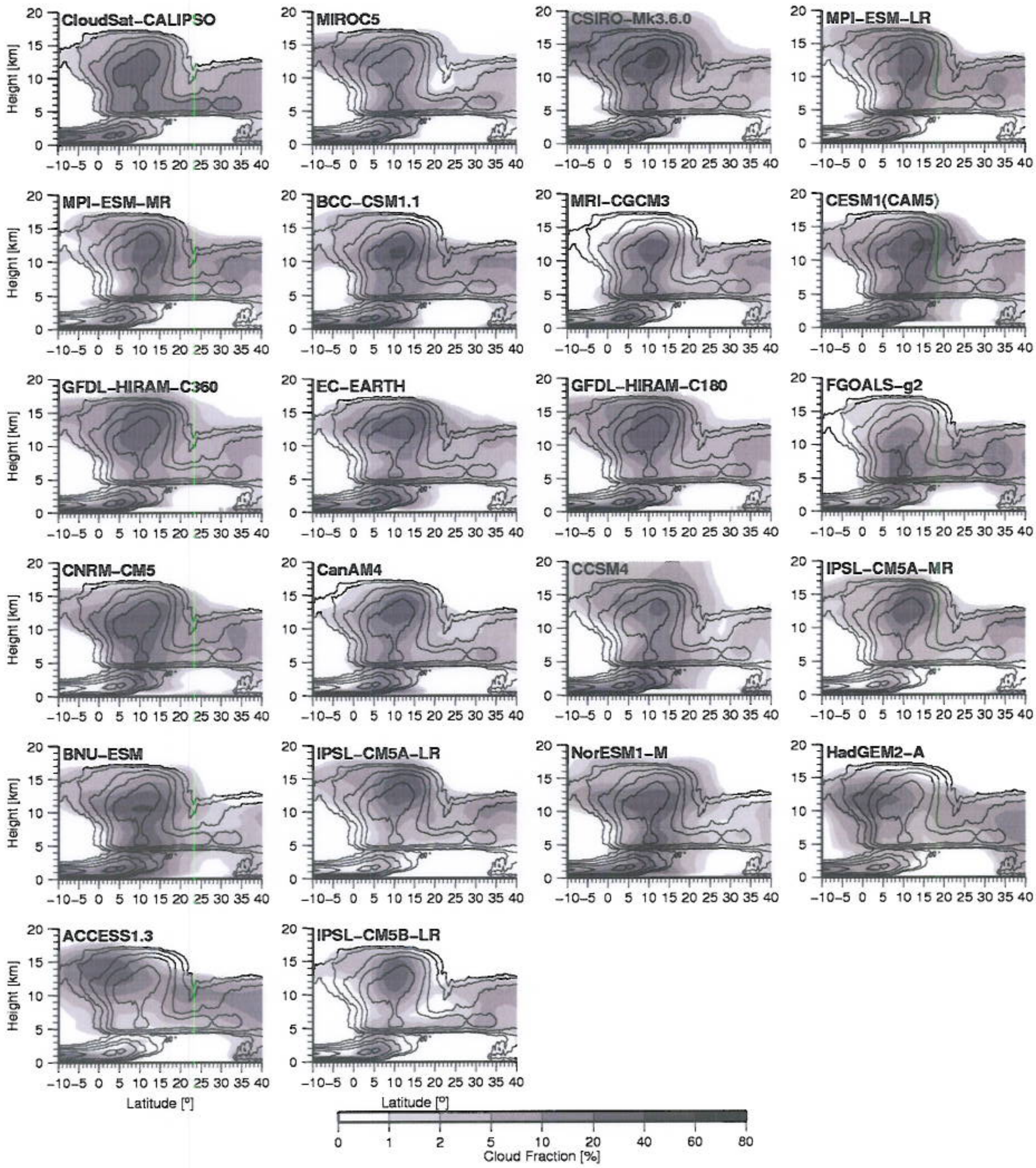

FIG. 8. Latitude-height diagrams of the cloud fraction averaged between 10°W-10°E, for the period JAS of the years 2006-2010 for the CloudSat-CALIPSO data set and 1979-2008 for the models. Models are organized from the warmest one over the Sahara [20°N–30°N, 10°W–10°E] (top left after the observation panel) to the coldest one (bottom right).

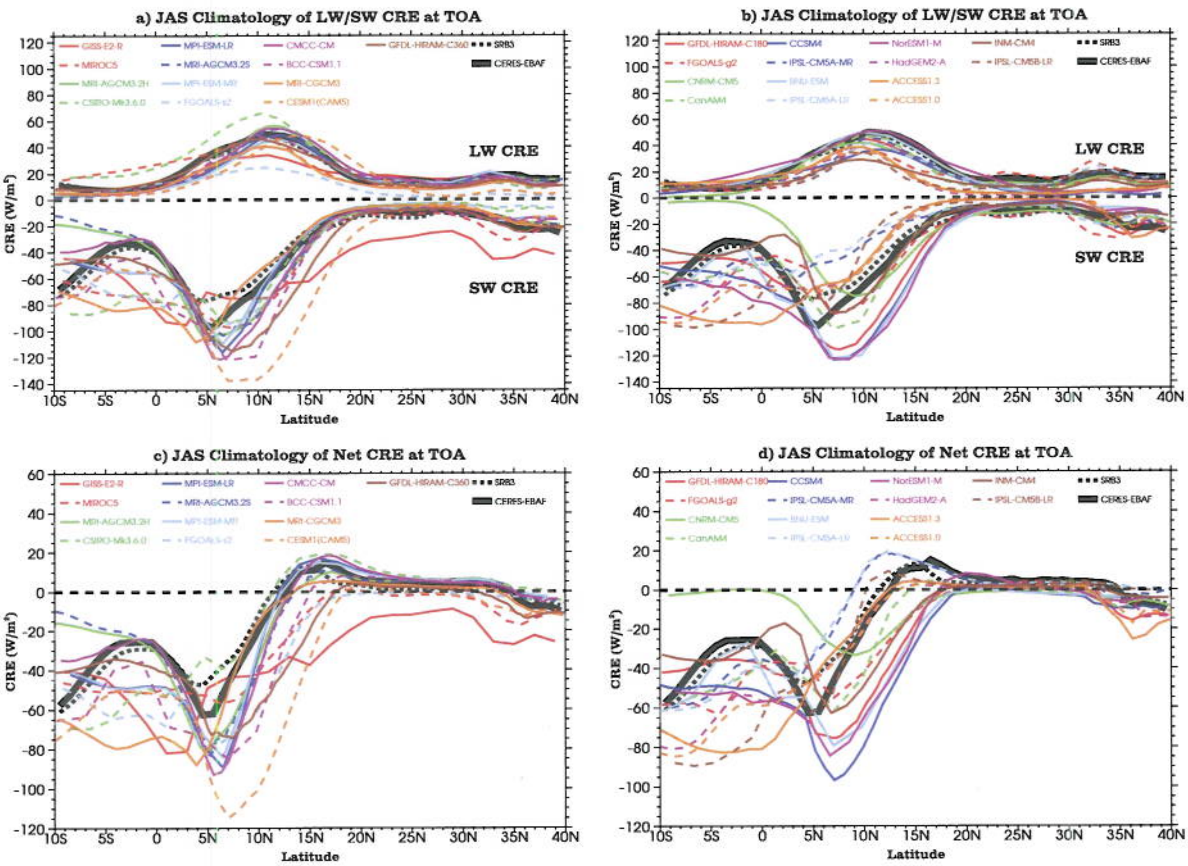

FIG. 9. a) and b) Cloud radiative effect (in W m^{-2}) at the top of the atmosphere in the SW (negative values) and LW (positive values) bands, averaged over 10°W-10°E, for the JAS period of the years 1979-2008. The left (right) panel corresponds to warmer (colder) models over the Sahara [20°N–30°N, 10°W–10°E]. c) and d) As in a) and b) respectively, but for the net CRE at the top of the atmosphere.

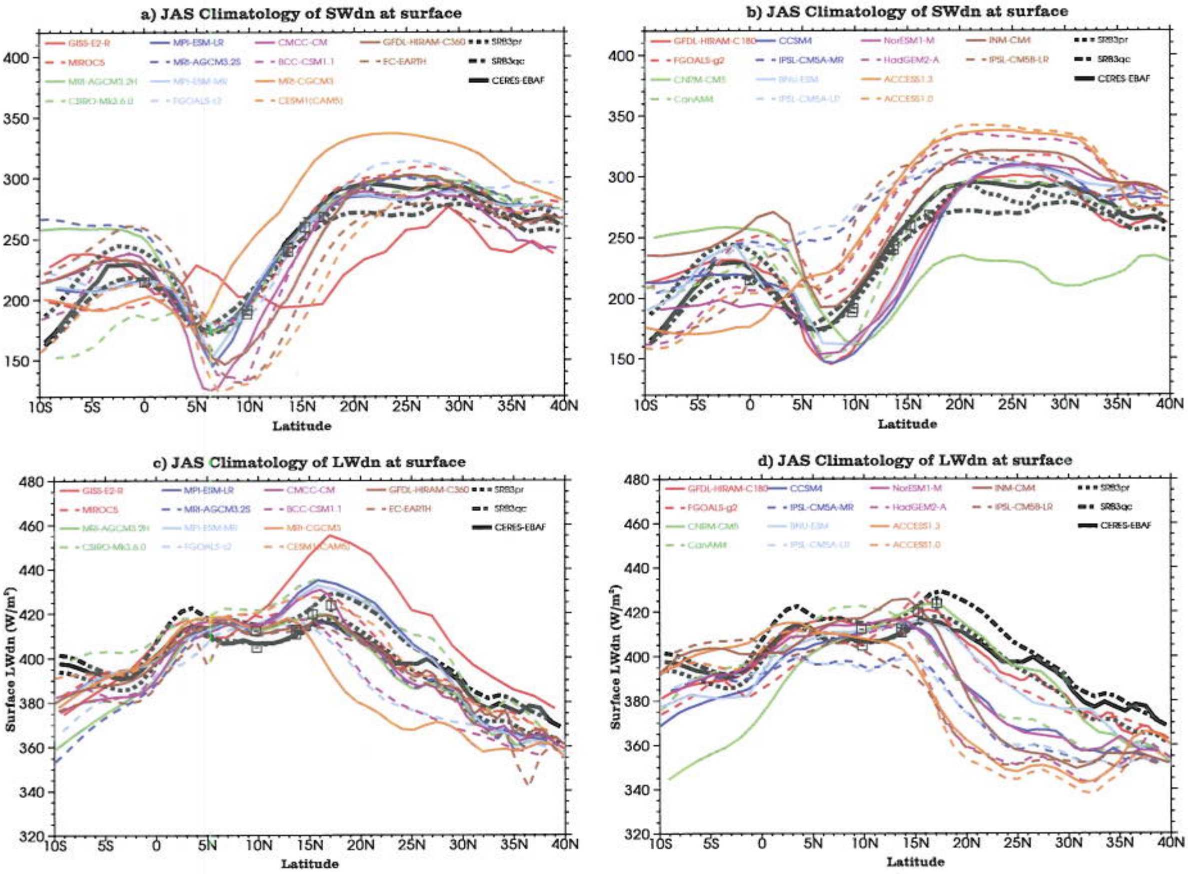

FIG. 10. a) and b) Downward shortwave radiative flux at the surface (in W m^{-2}), averaged over 10°W-10°E, for the JAS period of the years 1979-2008. The left (right) panel corresponds to warmer (colder) models over the Sahara [20°N–30°N, 10°W–10°E]. Mean fluxes for the sites along the transect (Table 3) together with their yearly minimum and maximum values are indicated. c) and d) As in a) and b) respectively, but for the downward longwave radiative flux at the surface.

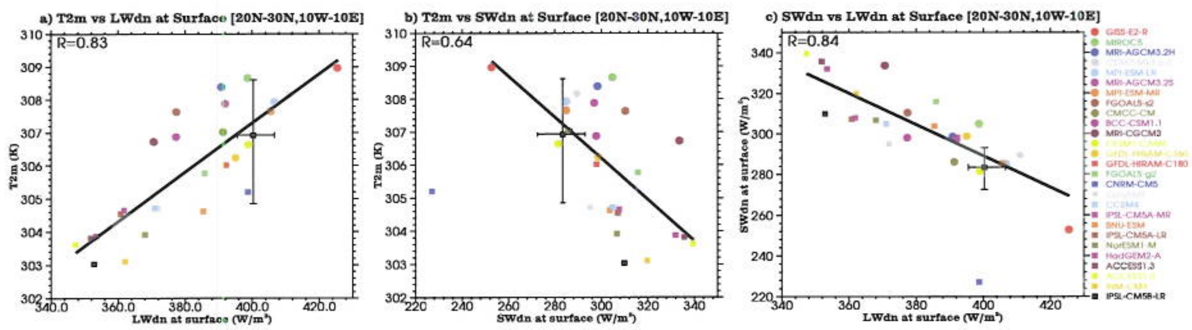

FIG. 11. a) Scatterplot of the downward longwave radiative flux at the surface (in W m^{-2}) against the 2-meter temperature (in K). Both variables are averaged over [20°N-30°N, 10°W-10°E], for the JAS period of the years 1979-2008. A linear regression was performed and its coefficient of determination is indicated in the top-left corner. b) As in a), but for the downward shortwave radiative flux at the surface against the 2-meter temperature. Note that the linear regression was performed without the CNRM-CM5 data. c) as in b) but for the downward longwave radiative flux at the surface against the downward shortwave radiative flux at the surface (in W m^{-2}). The black square with error bars indicates the mean obtained from observational datasets, i.e. SRB3pr, SRB3qc and CERES-EBAF for radiative fluxes, and ERAI, MERRA and CFSR for the 2-meter temperature. The warmer (colder) models are indicated with dots (filled square).

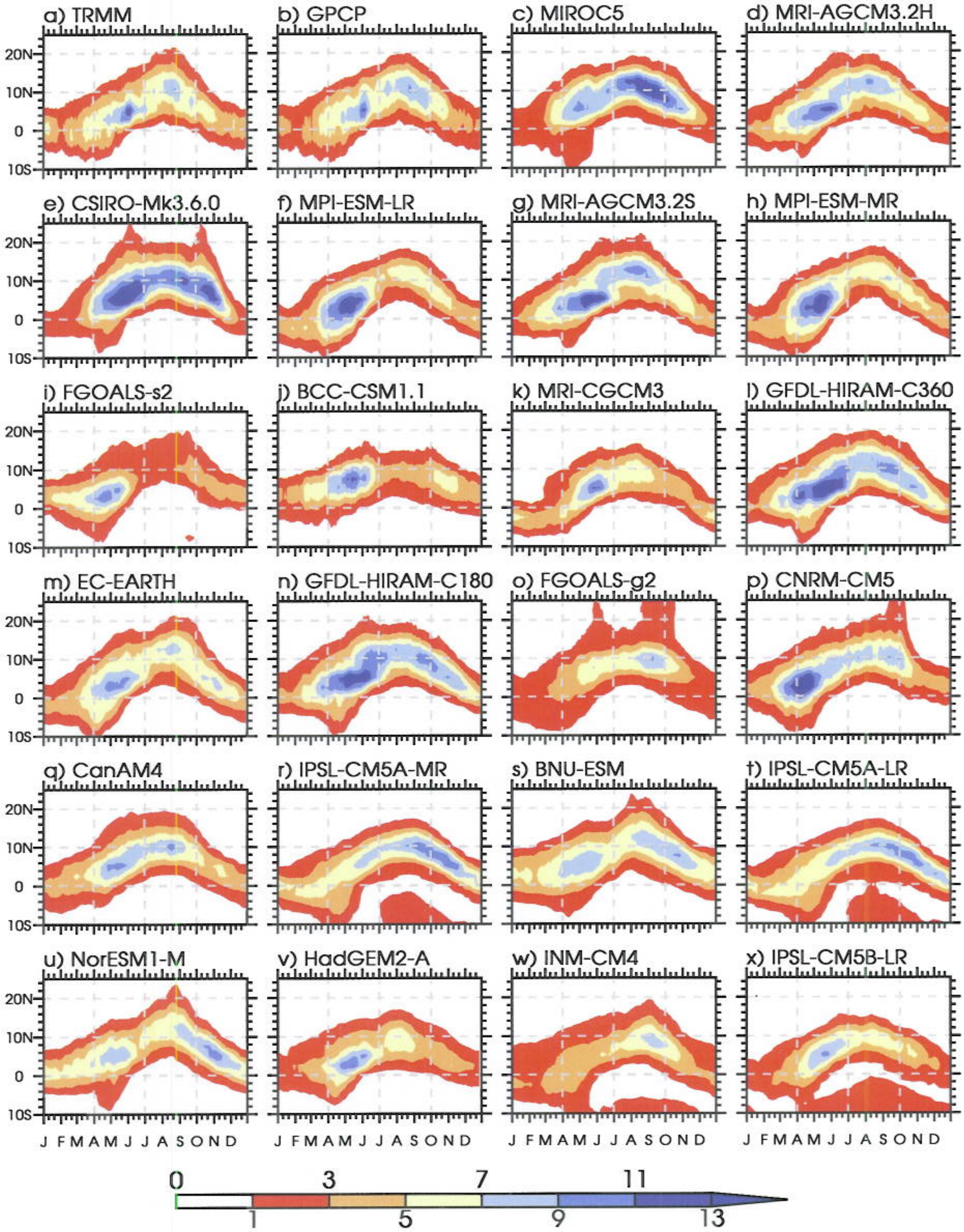

FIG. 12. Annual cycle of precipitation (in mm day^{-1}) averaged over 10°W-10°E. A 10-day running mean was performed on each dataset. Models are organized from the warmest one over the Sahara [20°N–30°N, 10°W–10°E] (top left after the observation panel) to the coldest one (bottom right).

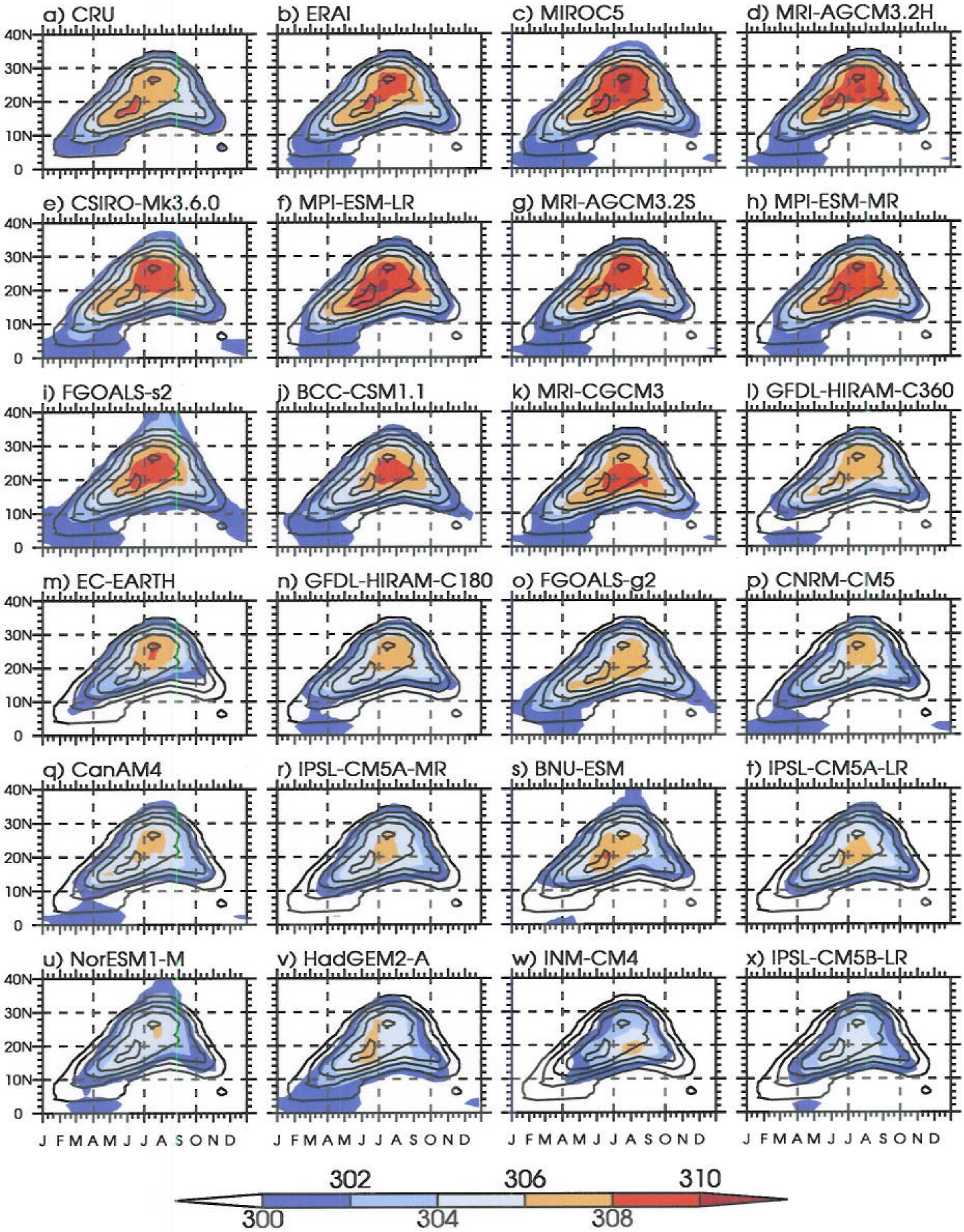

FIG. 13. Annual cycle of 2-meter temperature (in K) averaged over 10°W-10°E. Models are organized from the warmest one over the Sahara [20°N–30°N, 10°W–10°E] (top left after the observation panel) to the coldest one (bottom right).

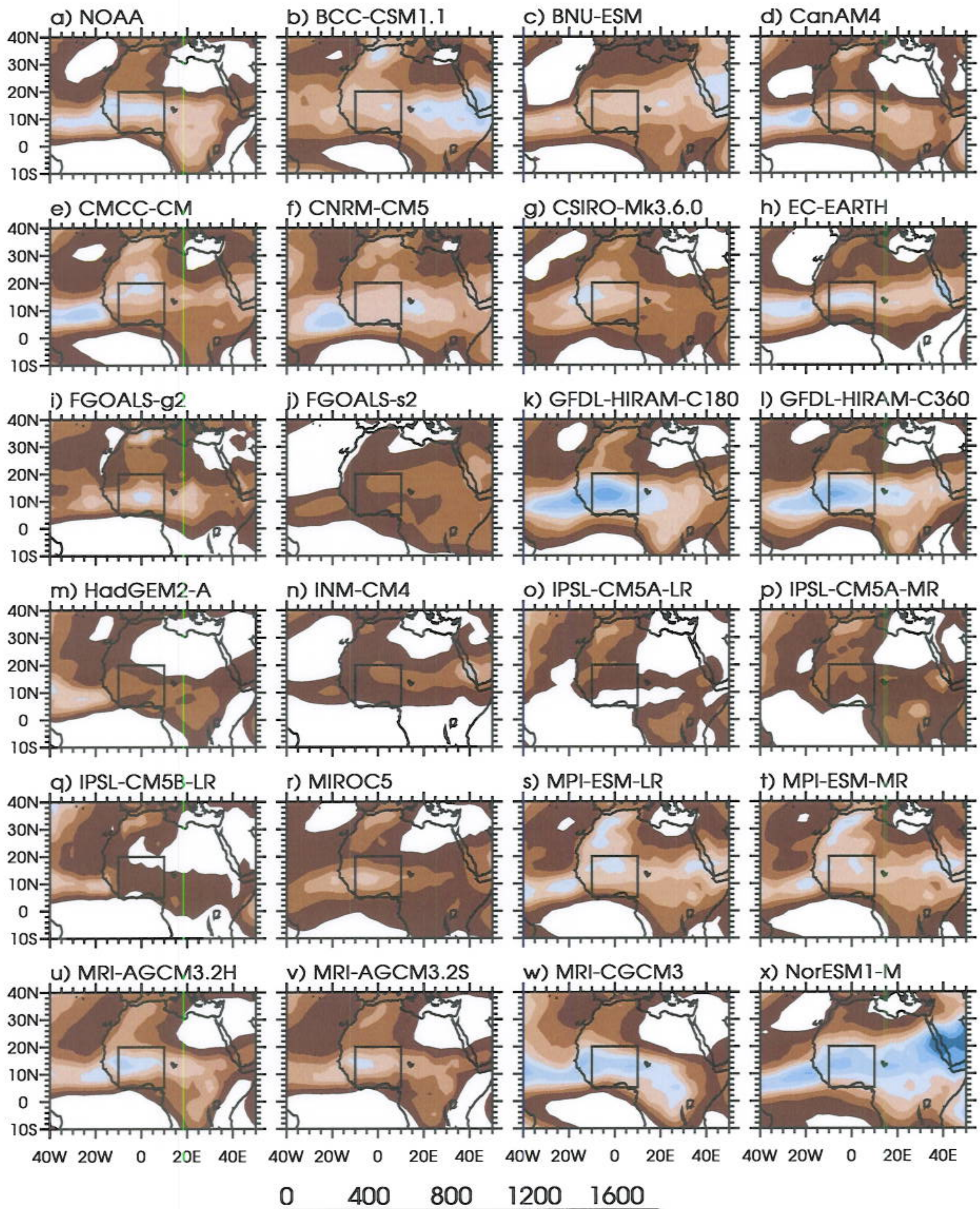

FIG. 14. Variance of OLR in the 1-90-day band, in W^2 m^{-4} for the JAS periods from 1979 to 2008. Daily OLR of CMIP5 models was regridded on the NOAA OLR grid (2.5°x2.5°), before computing filtered anomalies and their variance.

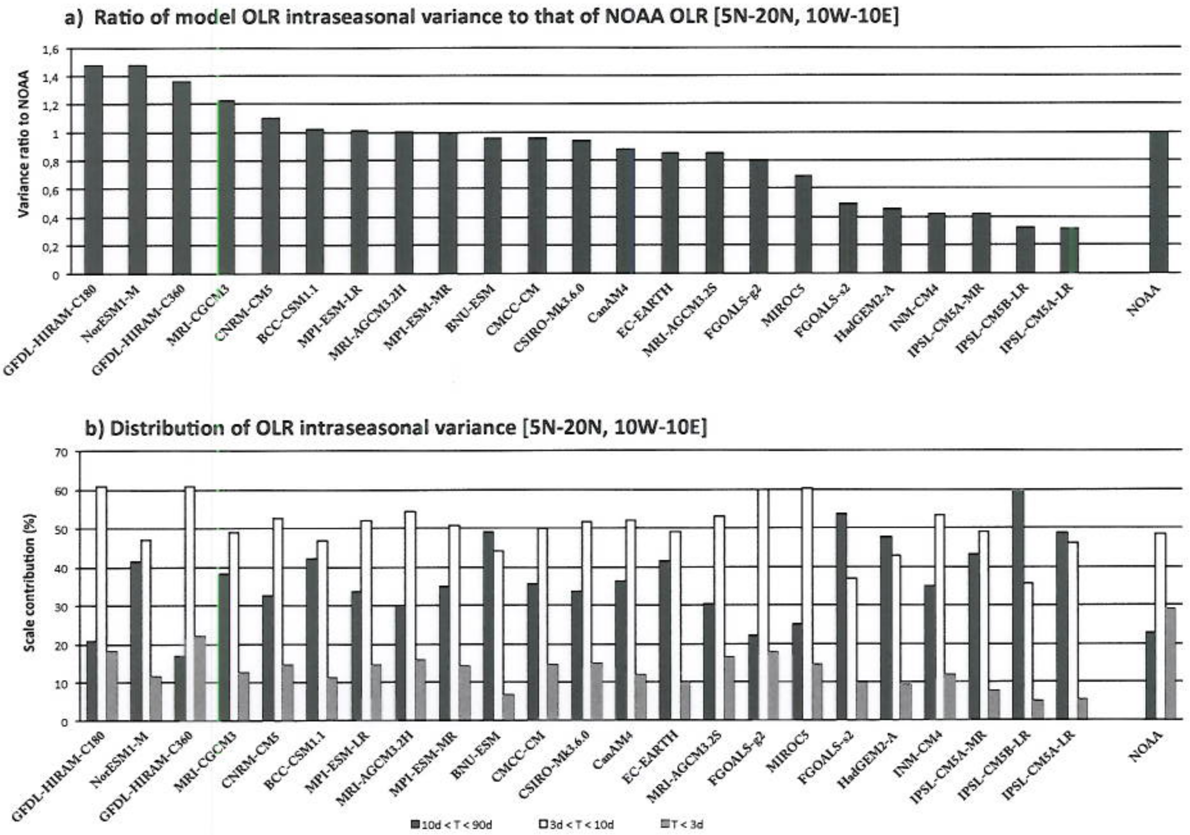

FIG. 15. a) Variance of OLR in the 1-90-day band averaged over the domain [5°N-20°N, 10°W-10°E], and for the JAS periods from 1979 to 2008. Values are normalized by the NOAA OLR variance. b) Distribution of the OLR intraseasonal variance (in %) across the 1-3-day (grey bars), 3-10-day (white bars) and 10-90-day (black bars) bands.

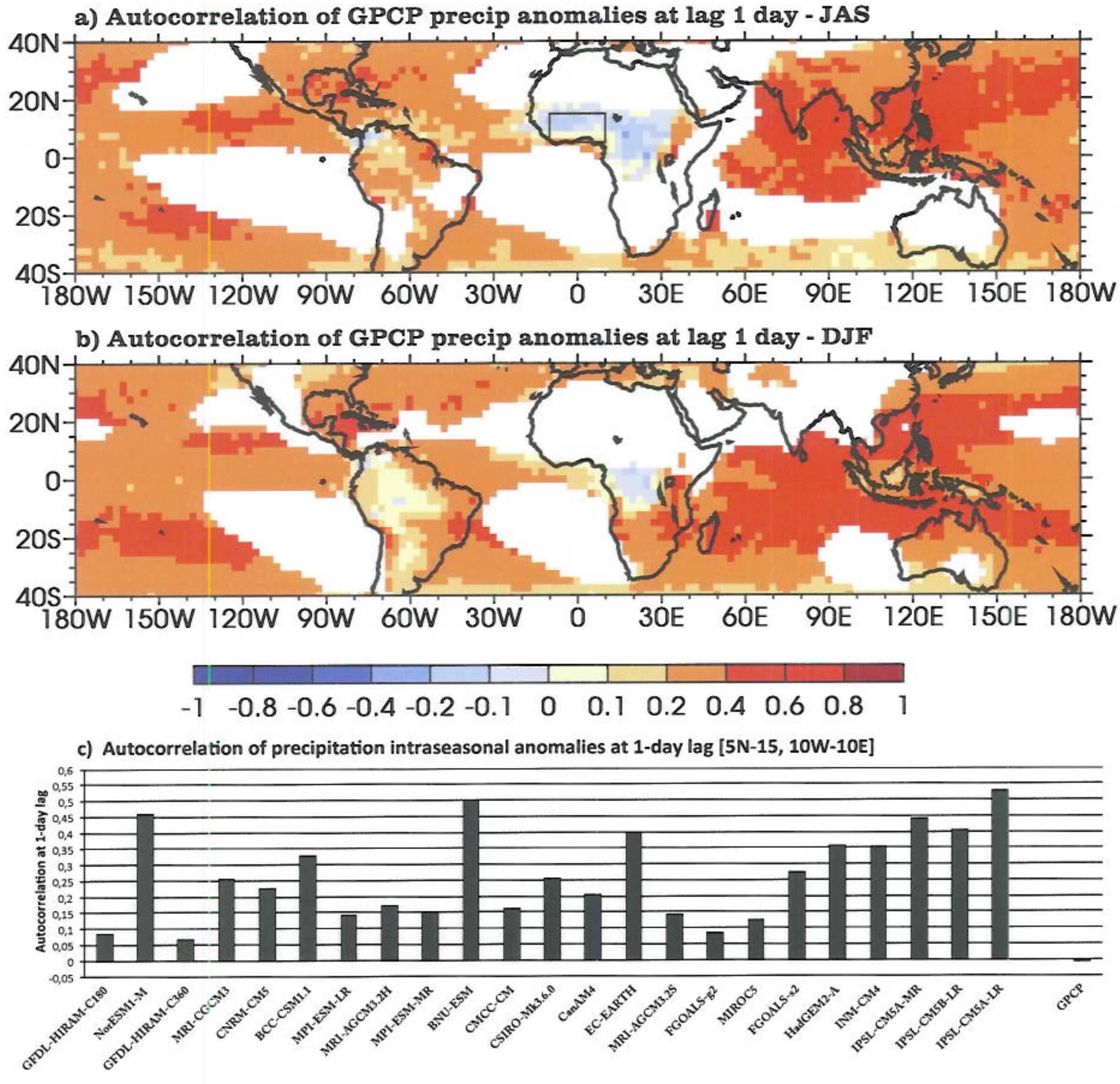

FIG. 16. a) Autocorrelation of a) JAS and b) DJF 1-90-day filtered precipitation at a 1-day lag for the GPCP daily dataset. Only grid-point where mean precipitation is greater than 1 mm day^{-1} are considered. c) Autocorrelation of 1-90-day filtered precipitation at a 1-day lag for GPCP and CMIP5 models, averaged over the domain [5°N-15°N,10°W-10°E]. Autocorrelation is computed for each JAS season of the period 1997-2008 for GPCP and 1979–2008 for CMIP5 model, and then averaged over all years. CMIP5 models and the GPCP dataset were regridded on the NOAA OLR grid before any computation.

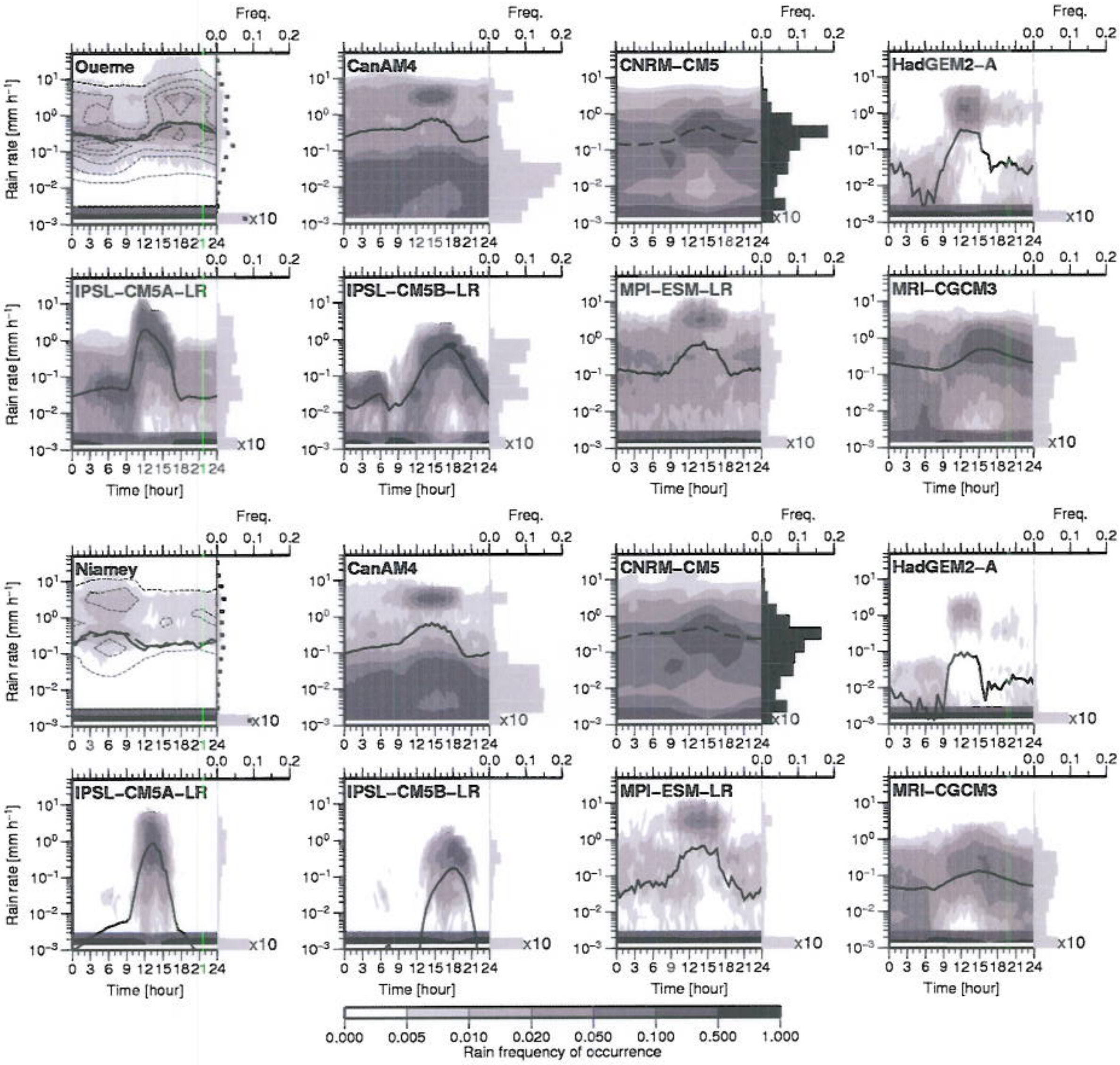

FIG. 17. Mean August diurnal cycle of precipitation intensity distribution (including null value). 1979-2008 is the period used for the models, 1999–2011 for the Ouémé site (2°E-9.5°N) and 1989–2011 for the Niamey site (2.2°E-13.5°N). The distribution is based on 30-min samples. The mean diurnal cycle of rainfall intensity is superimposed with the black line. Superimposed dashed lines also indicates the diurnal cycle of precipitation intensity distribution, but using 3-hourly samples for comparison with the CNRM-CM5 model.

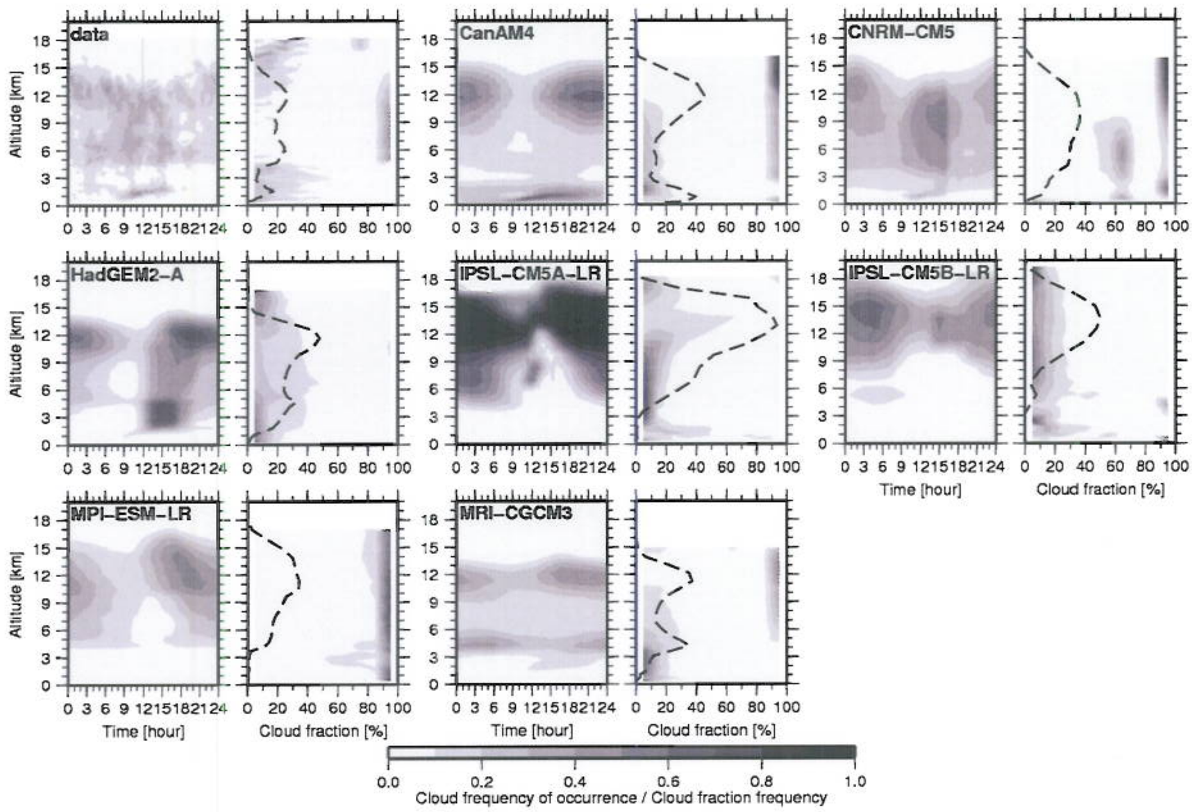

FIG. 18. As in Fig. 17 but for the August diurnal cycle of the cloud frequency of occurrence derived at the Niamey site (2.2°E-13.5°N). Observations comes from the AMF data acquired in 2006. The period 1979-2008 is used for the models. The vertical distribution of the cloud fraction is indicated on the right sub-panels. It is normalized at each level by the total cloud frequency of occurrence which is superimposed with the dashed line.